

## RESEARCH ARTICLE

# A fully implicit coupled pore-network/free-flow model for the pore-scale simulation of drying processes

K. Weishaupt<sup>a</sup> and T. Koch<sup>b</sup> and R. Helmig<sup>a</sup>

<sup>a</sup>Department of Hydromechanics and Modelling of Hydrosystems, University of Stuttgart, Germany; <sup>b</sup>Department of Mathematics, University of Oslo, Norway

## ARTICLE HISTORY

Compiled February 4, 2022

## ABSTRACT

We present a fully coupled pore-network/free-flow model providing pore-scale insight into drying processes. We solve the Navier-Stokes equations with component transport in the free-flow region, coupled to a dynamic two-phase, two-component pore-network model in the porous domain. The dynamic multi-physics model allows to temporally resolve drying processes in-between capillary equilibrium states. All simulations are non-isothermal and use pressure- and temperature-depended fluid properties. Carefully chosen coupling conditions and a monolithic solver ensure local conservation of mass, momentum and energy fluxes, in particular at the interface between both model domains. We solve for wetting and non-wetting fluid pressure fields and consider advective gas transport in the network. Numerical examples demonstrate that the coupled model is able to cover a wide range of physical processes relevant for drying and show the mutual interaction of the two subregions. The model is implemented in the modular open-source framework DuMu<sup>x</sup>such that extensions are straight-forward.

## KEYWORDS

dynamic pore-network model; multi-physics simulation; two-phase flow in porous media; evaporation and drying; pore-network Navier-Stokes coupling

## 1. Introduction

Drying processes are ubiquitous in environmental systems and technical applications. Understanding soil water evaporation (1) is crucial for agriculture and will become even more important with growing population and climate change, e.g, in connection with water scarcity or the salinization of soils (2). With the increased pressure of sustaining the population's demand for food, drying plays a key role for the conservation of perishable goods (3). Drying is one of the most energy-consuming process steps in many industrial applications (4) such that improvements in efficiency are needed more than ever to reduce global CO<sub>2</sub> emissions. Furthermore, dynamic markets susceptible to supply chain delays can be affected by long drying times.

---

This is an Accepted Manuscript of an article published by Taylor & Francis in Drying Technology on 04 Aug 2021 online and available online here: <https://doi.org/10.1080/07373937.2021.1955706>. It is deposited under the terms of the Creative Commons Attribution-NonCommercial License (<http://creativecommons.org/licenses/by-nc/4.0/>), which permits non-commercial re-use, distribution, and reproduction in any medium, provided the original work is properly cited.

CONTACT K. Weishaupt. Email: kilian.weishaupt@iws.uni-stuttgart.de

The need for better process understanding and optimization has fostered the development of a wide variety of mathematical and numerical models (5). Prat (6) laid the foundation for simulating drying processes with pore-network models (PNMs) by combining an invasion-percolation algorithm with a model for water vapor mass transport within the network. His model is widely used and has been extended to capture a large variety of physical processes and pore-scale mechanisms (7, 8). Such models usually consider the atmosphere adjacent to the porous medium by appropriate boundary conditions. For a better approximation of the atmospheric boundary layers, Shaeri et al. (9) coupled a gas-channel domain modeled by the Navier-Stokes equations to a porous domain modeled with a variant of the above-mentioned PNM. In their initial model and extended versions thereof (10, 11), the authors employ a pre-computed, time-invariant velocity field as basis for an advection-diffusion model in the gas channel coupled to diffusive vapor transport in the pore network. Advective gas flow driven by pressure gradients within the pore network is neglected. The model is isothermal and the quasi-static PNM can only resolve capillary equilibrium limiting applicability to slow drying processes.

The described models often focus on including a single or a limited number of physical process in addition to the two basic processes: capillary pressure-driven liquid flow and vapor diffusion in the gas phase (8).

In this work, we present a hybrid multi-physics model consisting of a dynamic two-phase PNM coupled with a single-phase free-flow model. It includes the two basic processes as well as the effects of liquid and gas viscosity, convection in the liquid and in the gas phase, enthalpy transport, and interaction with the atmosphere. Its key novelty lies in the relaxation of various assumptions made in the above-mentioned models and the generality and modularity of a fully-coupled monolithic solver approach (12–14) where the balance equations of both the free-flow domain and the pore-network model are assembled into one large system of equations. The latter is then solved simultaneously such that, in contrast to sequential coupling schemes (9–11), no coupling iterations are required, i.e., the individual subdomain models do not need to run and exchange coupling data repeatedly until convergence is reached. The dynamic PNM can temporally resolve all steps of the invasion and drying process including global mass redistribution due to local invasion events. The finite volume discretization in space and the implicit time discretization in combination with appropriate interface conditions and a monolithic solver scheme ensure local and global mass and energy conservation in each time step. By solving for the pressure and flow field in the entire domain, we can describe advective and diffusive species transport in the liquid and the gas phase occupying the pore space and the gas phase of the atmosphere. We consider a coupled energy balance equation in both the free flow and the PNM to capture non-isothermal effects such as the variation of density due to temperature gradients. The presented model is conceptually similar to the sharp interface model developed by Mosthaf (15), however they considered a Darcy-type model in the porous domain instead of a PNM. We remark here that pore-network models allow to model processes that cannot be captured in Darcy-scale continuum model such as the formation of isolated wetting fluid clusters and the loss of hydraulic connectivity, or the pore-scale interaction with the atmosphere. According to Metzger (8) and to the best of our knowledge, no PNM-based drying simulator has included convection in the gas phase up to now and the effects of liquid viscosity (16) and enthalpy transport (17) have not yet been presented in combination.

We consider these effects in a fully coupled way. Finally, we implement our model in the open-source framework DuMu<sup>x</sup>exploiting its modular structure. In combina-

tion with the monolithic solver based on numeric differentiation, model extensions are straight-forward. Effects like salt precipitation, nonlinear inertia-driven network flow or local thermal non-equilibrium (18) can be included without much implementation effort. We have recently presented our model concept including a small numerical example (19). In this work, we extend the physical complexity of the model by considering temperature-dependent surface tension and we improve the numerical robustness and performance of the model by using a more advanced way for solving the arising *nonlinear complementarity problem* given by Eq. (20). The main focus of this work, however, is the investigation of different physical aspects of the drying process by means of numerical experiments (now also featuring random pore-size distributions) which highlight the model's capabilities and the relevance to include certain physical processes such as pressure-driven, advective gas flow in the pore-network region which is very often neglected in other models.

## 2. Mathematical model and numerical implementation

We consider two computational domains: the porous region  $\Omega^{\text{PNM}}$  and the free-flow domain  $\Omega^{\text{FF}}$ . A two-phase, two-component pore-network model is used in  $\Omega^{\text{PNM}}$  while the single-phase two-component Navier-Stokes equations are solved in  $\Omega^{\text{FF}}$ . Both models are coupled at the common interface  $\Gamma$  and consider non-isothermal conditions and species transport. Gravity is neglected in both domains and local thermodynamic equilibrium is assumed.

The liquid wetting phase w consists of the main component water and the minor pseudo-component air. The gaseous non-wetting phase g is a mixture of air (main component) and water. Both phases w and g can be present in  $\Omega^{\text{PNM}}$  while only the gas phase g exists in  $\Omega^{\text{FF}}$ . We employ fluid properties based on constitutive relations and data provided by the industry standard IAPWS (20) and Reid (21). We assume a fixed contact angle of  $\theta = 0$  in this work such that the solid skeleton of the porous material is fully hydrophilic. Other contact angles could be considered by adapting the pore-local capillary-pressure saturation curve given by Eq. (16).

### 2.1. Free-flow model

In  $\Omega^{\text{FF}}$ , we solve the Navier-Stokes equations for compressible Newtonian fluids, neglecting gravity and dilation,

$$\frac{\partial(\varrho_g \mathbf{v}_g)}{\partial t} + \nabla \cdot (\varrho_g \mathbf{v}_g \mathbf{v}_g^T) = \nabla \cdot [\mu_g (\nabla \mathbf{v}_g + \nabla \mathbf{v}_g^T)] - \nabla p_g + \mathbf{f}, \quad (1)$$

where  $\varrho_g$  and  $\mu_g = \varrho_g \nu_g$  denote gas phase mass density and dynamic viscosity and  $\mathbf{v}_g$  and  $p_g$  are phase velocity and pressure.  $\mathbf{f}$  is an optional body force term. Solving Eq. (1) on three-dimensional domains, such as the free-flow channel considered in Section 3, can be computationally expensive. Our domain is horizontally thin, i.e., the channel width  $w_{\text{ch}}$  is much higher than its depth  $d_{\text{ch}}$  with an aspect ratio of  $w_{\text{ch}}/d_{\text{ch}} > 10$ . This makes it possible to solve Eq. (1) on a two-dimensional grid where we do not discretely resolve the channel depth anymore but instead consider a wall friction term (22, 23),

$$\mathbf{f} = -12 \frac{\mu_g}{d_{ch}^2} \mathbf{v}_g , \quad (2)$$

assuming a parabolic velocity profile along the neglected  $z$ -axis of  $\Omega^{FF}$ . When using this term, Eq. (1) in 2D describes the  $z$ -averaged velocity instead of the three-dimensional velocity. Of course, our model can be used for  $\Omega^{FF}$  discretized in 3D as well by just setting  $\mathbf{f} = 0$  which, however, comes at a higher computational cost.

Furthermore, we consider one molar balance equation for each component  $\kappa \in \{\text{water, air}\}$ :

$$\frac{\partial(x_g^\kappa \varrho_{\text{mol},g})}{\partial t} + \nabla \cdot (x_g^\kappa \varrho_{\text{mol},g} \mathbf{v}_g + \mathbf{j}_{\text{diff,mol},g}^{\kappa,FF}) = q^\kappa , \quad (3)$$

where  $x_g^\kappa$  is the mole fraction of component  $\kappa$  within the gas phase and  $\varrho_{\text{mol},g}$  is the molar density of the latter.  $q^\kappa$  is a molar sink or source term which is zero in this work. The diffusive molar flux  $\mathbf{j}_{\text{diff,mol},g}^{\kappa,FF}$  is approximated by Fick's first law,

$$\mathbf{j}_{\text{diff,mol},g}^{\kappa,FF} = -\frac{1}{M^\kappa} \varrho_g D_g \nabla X_g^\kappa , \quad (4)$$

where  $D_g$  is the binary diffusion coefficient for water and air within the gas phase and  $X_g^\kappa$  is the mass fraction of component  $\kappa$ . Since Eq. (1) yields a mass-averaged bulk velocity (24), we consider a mass-based form of Fick's law here such that the diffusive mass flux needs to be converted into a molar flux by division by the molar mass  $M^\kappa$ . The mass fraction can be expressed in terms of mole fractions,

$$X_\alpha^\kappa = \frac{x_\alpha^\kappa M^\kappa}{M_\alpha} = \frac{x_\alpha^\kappa M^\kappa}{\sum_{\kappa'} x_\alpha^{\kappa'} M^{\kappa'}} , \quad (5)$$

where  $M_\alpha$  is the phase-averaged molecular weight. Note that  $\sum_\kappa x_\alpha^\kappa = \sum_\kappa X_\alpha^\kappa = 1$ .

The energy balance is given by

$$\frac{\partial(\varrho_g u_g)}{\partial t} + \nabla \cdot (h_g \varrho_g \mathbf{v}_g) + \sum_\kappa \nabla \cdot (\mathbf{j}_{\text{diff,mol},g}^{\kappa,FF} h_g^\kappa) - \nabla \cdot (\lambda_g \nabla T) = q^e , \quad (6)$$

where  $u_g$  is the specific internal energy and  $h_g$  is the specific phase enthalpy. The phase enthalpy can be expressed as the sum

$$h_g = \sum_\kappa X_g^\kappa h_g^\kappa , \quad (7)$$

where  $h_g^\kappa$  denotes the specific enthalpy of a phase containing only component  $\kappa$ .

The term  $\mathbf{j}_{\text{diff,mol},g}^{\kappa,FF} h_g^\kappa$  in Eq. (6) accounts for the molar diffusive energy transport. Heat conduction is described by Fourier's law, where  $\lambda_g$  is the effective thermal conductivity of the gas phase and  $T$  the temperature. Finally,  $q^e$  is an energy sink or source term which is zero in this work.

We discretize Eqs. (1) to (6) with a staggered-grid finite volume approach, also known as MAC scheme (25). This yields stable and oscillation-free solutions without

the need of any stabilization (26). All scalar primary variables ( $p_g$ ,  $x_g^{\text{water}}$  and  $T$ ) are located at the primal grid control volume centers while normal-velocity degrees of freedom ( $\mathbf{v}_g \cdot \mathbf{n}$ ) live on the dual grid control volume centers, constructed around the face centers of the primal grid (27).

## 2.2. Pore-network model

In  $\Omega^{\text{PNM}}$ , we employ a dynamic PNM with two miscible fluid phases, including component and energy transport, and phase change. We consider two individual phase pressures  $p_w$  and  $p_g$ . Note that instead of using a semi-implicit solution strategy (28, 29), where the pressure and saturation fields are solved for sequentially, we consider a fully coupled and implicit model formulation such that all balance equations are solved simultaneously. Figure 1(a) schematically depicts two pore bodies connected by a pore throat and shows the relevant pore space dimensions. In this work, we consider cubic pore bodies connected by throats of either circular, square or triangular cross-sectional areas as shown in Fig. 1(b).

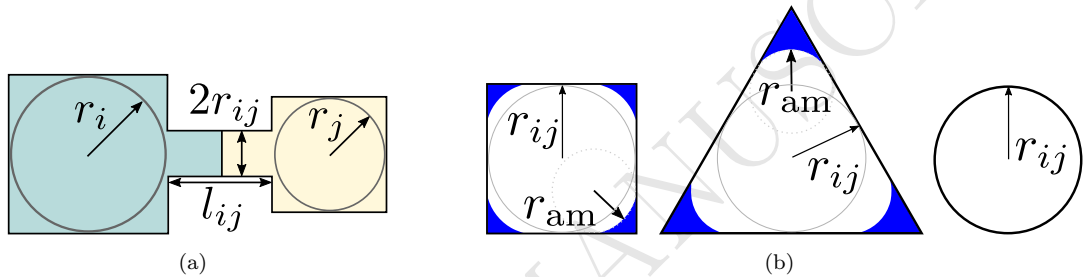


**Figure 1.** Pore-body and pore-throat geometry. (a) Two pore bodies connected by a pore throat.  $r_i$  and  $r_j$  are the inscribed pore body radii and can be chosen independently (they can also be equal).  $l_{ij}$  is the length of the throat connecting pores  $i$  and  $j$ . The inscribed throat radius  $r_{ij}$  is determined as described in Appendix B. The left pore body features a volume  $V_i$  marked in green which includes half of the pore throat volume. The same applies for  $V_j$  highlighted in yellow. (b) Throat cross-sectional shapes and wetting layers facilitating corner flow. In this figure, each throat has the same inscribed radius  $r_{ij}$ . Wetting-phase layers (blue) may occur in angular throats after the non-wetting phase has invaded the throat.  $r_{am}$  is the radius of curvature of the layer's arc meniscus.

### 2.2.1. Balance equations

Assuming fully developed creeping flow,

$$Q_{\alpha,ij} = g_{\alpha,ij}(p_{\alpha,i} - p_{\alpha,j}) \quad (8)$$

describes the volume flow rate of phase  $\alpha \in \{w, g\}$  through pore throat  $ij$  connecting pore bodies  $i$  and  $j$  (28). The pore throat transmissibility  $g_{\alpha,ij}$  of phase  $\alpha$  depends on the throat geometry, the throat-local capillary pressure and the fluid viscosity.  $p_{\alpha,i}$  and  $p_{\alpha,j}$  are the pore phase pressures of two neighboring pores  $i$  and  $j$ . In the presence of only one single phase,  $g_{\alpha,ij}$  is given by (30)

$$g_{\alpha,ij} = \frac{k A_{\text{tot},ij}^2 G}{\mu_\alpha l_{ij}}, \quad (9)$$

where  $A_{\text{tot},ij}$  is the total cross-sectional area of the throat and  $l_{ij}$  its effective length, defined here as the Euclidean pore-body-center distance minus the inscribed pore-body

radii  $r_i$  and  $r_j$ . The dimensionless shape factor is given by (31)

$$G = \frac{A_{\text{tot},ij}}{P_{\text{tot},ij}^2}, \quad (10)$$

with the throat cross-sectional perimeter  $P_{\text{tot},ij}$  and a shape-dependent constant  $k$  (0.6, 0.5623 and 0.5 for equilateral triangles, squares and circles, respectively). We neglect the pore-body pressure loss so that the flow resistance is fully determined by the throat.

In the presence of both phases (angular throats), the transmissibility of the wetting layer is given by (32),

$$g_{w,ij} = \frac{r_{\text{am}}^2}{\mu_w l_{ij}} \sum_{\Lambda=1}^{n_{\text{corner}}} \frac{A_{w,\Lambda}}{\xi_{\Lambda}}. \quad (11)$$

The radius of curvature of the arc menisci is denoted by  $r_{\text{am}} = \gamma/p_c$  (the ratio of interfacial tension and capillary pressure),  $A_{w,\Lambda}$  is the cross-sectional area of the wetting layer in corner  $\Lambda$ , and  $\xi_{\Lambda}$  is a dimensionless resistance factor (33). The conductance of the non-wetting gas phase as the throat's lumen is given by (34)

$$g_{g,ij} = \frac{r_{\text{eff}}^2 A_{g,ij}}{8\mu_g l_{ij}}, \quad r_{\text{eff}} = \frac{1}{2} \left( \sqrt{\frac{A_{g,ij}}{\pi}} + r_{ij} \right), \quad (12)$$

where  $A_{g,ij}$  is the gas phase cross-sectional area and  $r_{ij}$  denotes the inscribed radius of the pore throat.

Given a pore fully saturated with the wetting phase, an entry capillary pressure needs to be overcome before the gas phases can invade a pore throat (35, 36). If the capillary pressure falls below a certain threshold pressure, snap-off occurs and the pore throat is fully saturated by the wetting phase again. Entry and snap-off pressures are given in Appendix A. As described later in Section 2.2.3 and Fig. 3, we check for invasion or snap-off at each throat after each Newton iteration.

We formulate a molar balance for each component  $\kappa$  for each pore  $i$ ,

$$\begin{aligned} V_i \frac{\partial(\sum_{\alpha} (x_{\alpha,i}^{\kappa} \varrho_{\text{mol},\alpha} S_{\alpha,i}))}{\partial t} &+ \sum_{\alpha} \sum_j (x_{\alpha,i}^{\kappa} \varrho_{\text{mol},\alpha} Q_{\alpha})_{ij} \\ &+ \sum_{\alpha} \sum_j \left( j_{\text{diff,mol},\alpha}^{\kappa, \text{PNM}} A_{\alpha} \right)_{ij} = (V q^{\kappa})_i, \end{aligned} \quad (13)$$

where  $V_i$  is the volume of pore  $i$ ,  $x_{\alpha,i}^{\kappa}$  is the mole fraction of component  $\kappa$  within phase  $\alpha$ ,  $\varrho_{\text{mol},\alpha,i}$  is the molar density and  $S_{\alpha,i}$  the pore-local saturation of phase  $\alpha$ . For interface pores, the source term  $(V q^{\kappa})_i$  is non-zero and accounts for the mass exchange with  $\Omega^{\text{FF}}$  as given by Eq. (27). We equally distribute the throat volume  $A_{\text{tot},ij} l_{ij}$  to the adjacent pore body volumes  $V_i$  and  $V_j$  as shown in Fig. 1(a). In analogy to Eq. (4), Fick's first law is used to describe diffusive fluxes in the PNM,

$$j_{\text{diff,mol},\alpha,ij}^{\kappa, \text{PNM}} = \frac{1}{M^{\kappa}} \frac{\varrho_{\alpha,i} + \varrho_{\alpha,j}}{2} \frac{D_{\alpha,i} + D_{\alpha,j}}{2} \frac{X_{\alpha,i}^{\kappa} - X_{\alpha,j}^{\kappa}}{l_{ij}}. \quad (14)$$

We consider the following energy balance equation for each pore body (assuming local thermodynamic equilibrium),

$$\begin{aligned} V_i \frac{\partial(\sum_{\alpha} (\varrho_{\alpha} u_{\alpha} S_{\alpha})_i)}{\partial t} + \sum_{\alpha} \sum_j (\varrho_{\alpha} h_{\alpha} Q_{\alpha})_{ij} \\ + \sum_{\alpha} \sum_j \left[ A_{\alpha,ij} \sum_{\kappa} \left( j_{\text{diff,mol},\alpha}^{\kappa,\text{PNM}} h_{\alpha}^{\kappa} \right)_{ij} \right] \\ + \sum_{\alpha} \sum_j \frac{\lambda_{\alpha,i} + \lambda_{\alpha,j}}{2} \frac{T_i - T_j}{l_{ij}} A_{\alpha,ij} = (Vq^e)_i . \end{aligned} \quad (15)$$

As for the free-flow domain, the term  $j_{\text{diff,mol},\alpha}^{\kappa,\text{PNM}} h_{\alpha}^{\kappa}$  takes into account the molecular diffusive energy transport. We note that due to phase change and  $h_g^{\kappa} > h_w^{\kappa}$ , we see a temperature drop during evaporation (enthalpy of vaporization). For interface pores, the source term  $(Vq^e)_i$  is non-zero but accounts for the energy exchange with  $\Omega^{\text{FF}}$  as given by Eq. (30).

We only balance energy fluxes within the pore space (the fluid) here, assuming a perfectly insulating solid matrix. We have recently developed a dual network concept (18) in order to include heat conduction in the solid phase. There, a fluid network (representing the void space as in classical pore-network modeling) is coupled to a second, solid network via appropriate pore-local sink and source terms allowing the description of local thermal non-equilibrium effects. We aim to incorporate this concept into the model presented here in future work.

### 2.2.2. Closure relations and phase composition

The presented two-phase two-component system is fully determined by the following closure relations. In the presence of two fluid phases, we require  $S_{w,i} + S_{g,i} = 1$  (no void space) and  $x_{\alpha,i}^{\text{water}} + x_{\alpha,i}^{\text{air}} = 1$ .

The pore-local  $p_c - S_w$  relation for cubic pore bodies is chosen as (28)

$$p_{c,i}(S_{w,i}) = \frac{2\gamma}{r_i(1 - \exp(-6.83S_{w,i}))} , \quad (16)$$

where  $r_i$  is the inscribed radius of pore body  $i$  and  $\gamma$  is the interfacial tension. We only consider cubic pore bodies here but the model is open for extension by adapting Eq. (16). For sake of numerical robustness, we regularize Eq. (16) such that the curve becomes linear for  $S_{w,i} < 1 \times 10^{-2}$  and we enforce  $p_{c,i}(S_{w,i} = 1) = 0$ . This is done by linearly connecting  $p_{c,i}(S_{w,i} = 1 - 1 \times 10^{-6})$  with  $p_{c,i}(S_{w,i} = 1)$ . The extreme negative slope of the curve leads to very high negative values of  $p_{c,i}(S_{w,i} > 1)$  resulting in a sort of penalization for nonphysical saturation values above one and leading to improved Newton convergence behavior (Section 2.3.2). Furthermore, we require the numerical solver to fulfill  $0 \leq S_{\alpha,i} \leq 1$  once the Newton scheme is converged.

Evaporation and condensation are not modeled explicitly (37) as we assume local thermodynamic equilibrium in each pore body such that the phase composition can be determined implicitly. We denote the component fugacities by  $f_{\alpha}^{\kappa} = f^{\kappa}$ . Assuming air as ideal gas, Raoult's law,

$$p_g^{\text{water}} = f^{\text{water}} = x_w^{\text{water}} p_{\text{sat}}^{\text{water}} , \quad (17)$$

and Henry's law,

$$p_g^{\text{air}} = f^{\text{air}} = x_w^{\text{air}} H , \quad (18)$$

are used to calculate the phase composition. The symbol  $p_g^\kappa = p_g x_g^\kappa$  denotes the partial pressure of component  $\kappa$  in the gas phase,  $p_{\text{sat}}^{\text{water}}$  is the saturated vapor pressure and  $H$  is the temperature-dependent Henry coefficient. We take into account the reduction of  $p_{\text{sat}}^{\text{water}}$  due to capillary effects (38),

$$p_{\text{sat},\text{Kelvin}}^\kappa = p_{\text{sat}}^\kappa \exp \left( -\frac{p_c M^\kappa}{\varrho_w R T} \right) . \quad (19)$$

A phase  $\alpha$  may completely vanish, e.g., if a pore dries out or gets filled with water. This leads to the degeneration of the two-phase system such that  $S_\alpha$  and  $x_\alpha^\kappa$  are deprived of their physical meaning. One possibility to account for this is a local, adaptive change of primary variables (39, 40) which is, however, not always numerically stable. We consider a different approach where an additional pore-local constraint for each phase  $\alpha$  is formulated (41), the so-called *nonlinear complementarity problem* (NCP):

$$S_{\alpha,i} \left( 1 - \sum_\kappa x_{\alpha,i}^\kappa \right) = 0 \quad \wedge \quad 1 - \sum_\kappa x_{\alpha,i}^\kappa \geq 0 \quad \wedge \quad S_{\alpha,i} \geq 0 . \quad (20)$$

We solve Eq. (20) using a penalized *Fischer-Burmeister* function (42)

$$\lambda_{\text{FB}} \left( \sqrt{a^2 + b^2} - (a + b) \right) + (1 - \lambda_{\text{FB}})(\max(0, a) \max(0, b)) = 0 \quad (21)$$

with  $a = S_{\alpha,i}$  and  $b = 1 - \sum_\kappa x_{\alpha,i}^\kappa$ . Following the authors' suggestion, we set the parameter  $\lambda_{\text{FB}}$  to 0.95 (which improved Newton convergence in comparison with the non-penalized version,  $\lambda_{\text{FB}} = 1$ ). We observed that Eq. (21) leads to faster and more stable Newton convergence compared to

$$\min(S_{\alpha,i}, 1 - \sum_\kappa x_{\alpha,i}^\kappa) = 0 \quad (22)$$

which we used previously (19) for solving Eq. (20).

### 2.2.3. Primary variables and numerical model

The PNM's primary variables are the wetting-phase saturation  $S_w$ , the component fugacities  $f^{\text{air}}$  and  $f^{\text{water}}$ , the fluid temperature  $T$  and a phase pressure  $p_\alpha$ . The latter is either  $p_w$  or  $p_g$ , depending on the pore-local  $S_{w,i}$ . We found that this very simple switching mechanism increases the model's numerical robustness for  $S_w \rightarrow 0$ . In this paper, we chose a threshold of  $S_{w,i} = 0.1$  below which  $p_w$  is replaced by  $p_g$ .

We use a dynamic and fully coupled PNM which yields the phase saturations and pressures (along with the above-mentioned other primary variables) simultaneously. As explained later in Section 2.3.2 and Fig. 3, a Newton-Raphson method is used to solve the global system of equations resulting from the coupling of  $\Omega^{\text{FF}}$  with  $\Omega^{\text{PNM}}$ . The invasion state of each pore-throat (see Eqs. (A1) and (A4)) is checked after each

global Newton iteration and the constitutive laws for  $g_{\alpha,ij}$  are adapted accordingly. If  $p_{c,i}$  exceeds  $p_{c,e}$  in a previously water-filled throat, the latter is marked as invaded, while a snap-off event occurs if  $p_{c,i}$  falls below  $p_{c,s}$  for invaded throats. We enforce at least one additional Newton iteration if invasion or snap-off occurred. We refer to Chen (43), who independently developed a very similar approach, for further details.

### 2.3. Interface conditions

The continuity of mass, momentum and energy at the interface between the free flow and the pore-network model is enforced by means of appropriate coupling conditions, assuming creeping flow at the interface. For this, we revised the REV-scale coupling conditions proposed by Mosthaf (15) and adapted them for the pore scale. Interfacial quantities of the free-flow domain are marked by  $[.]^{\text{FF}}$ , while  $[.]^{\text{PNM}}$  refers to the quantities of the pore-network model, respectively. We define a unit vector  $\mathbf{n}$  normal to the coupling interface which points out of the own model domain.

In contrast to REV-scale coupled models (15), where fluxes are exchanged across the entire common surface between the free-flow and porous-medium  $\Gamma$ , we only consider discrete, local pore-scale coupling interfaces  $\Gamma_i$  which correspond to pore bodies intersecting with the free-flow domain  $\Omega^{\text{FF}}$  as shown in Fig. 2.

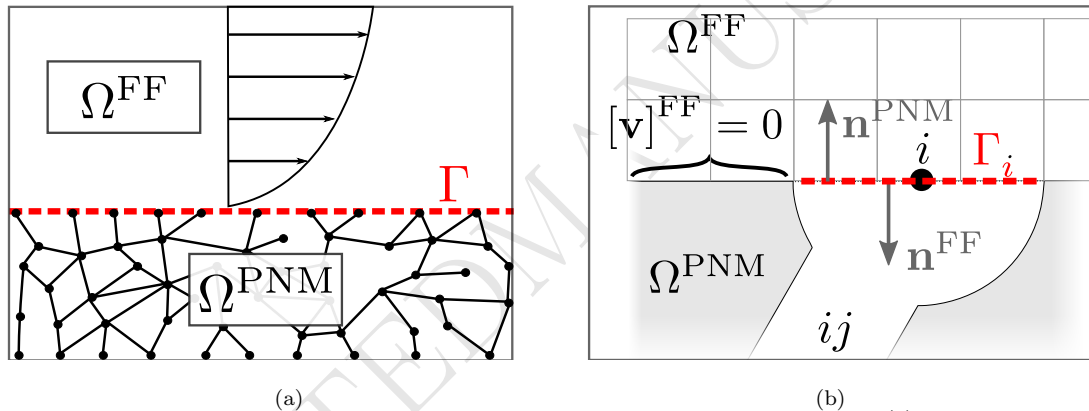


**Figure 2. Coupling free-flow and pore-network model: interface conditions.** (a) The free-flow domain  $\Omega^{\text{FF}}$  and the pore-network model domain  $\Omega^{\text{PNM}}$  are separated by  $\Gamma$ . (b)  $\Gamma_i$  is a pore-local coupling interface (here with three free-flow cells per pore-width). Figure taken from (19) (license: CC BY 4.0).

The interface cuts each coupling pore body  $i$  in half and we only consider the interior volume. We restrict the coordination number of said pore bodies to one such that only one pore throat is attached to them. This limitation, facilitating the formulation of coupling conditions, could be addressed in future work. Each coupling interface  $\Gamma_i$  is connected with at least one free-flow grid cell positioned matching above the pore. Figure 2(b) schematically shows the coupling of one pore body with three free-flow grid cells. We assume no-slip/no-flow conditions for  $\Omega^{\text{FF}}$  for the solid grain locations (marked gray in Fig. 2), such that  $\mathbf{v}_g = 0$  on  $\Gamma \setminus \Gamma_i$ .

#### 2.3.1. Coupling conditions

The momentum interface conditions are formulated for the creeping flow regime (13). Assuming mechanical equilibrium at  $\Gamma_i$ ,

$$[p_g]^{\text{FF}} = [p_g]^{\text{PNM}} \quad \text{on } \Gamma_i \quad (23)$$

is enforced for the normal force component.

The tangential momentum exchange in terms of pore-scale slip is given by

$$[\mathbf{v}_g \cdot \mathbf{t}_k]^{\text{FF}} = \begin{cases} v_{\text{slip},k} & \text{on } \Gamma_i, \\ 0 & \text{else,} \end{cases} \quad (24)$$

with

$$v_{\text{slip},k} = \frac{1}{\beta_{\text{pore}}} [(-(\nabla \mathbf{v}_g + \nabla \mathbf{v}_g^T) \cdot \mathbf{n}) \cdot \mathbf{t}_k]^{\text{FF}} + [\mathbf{v}_g \cdot \mathbf{t}_k]^{\text{PNM}}, \quad (25)$$

where  $\mathbf{t}_k$ ,  $k \in \{0, \dots, d-1\}$  spans the interface's tangent plane. The tangential component of the pore-body interface velocity satisfies

$$[\mathbf{v}_g \cdot \mathbf{t}_k]^{\text{PNM}} = \frac{Q_{g,ij}}{|\Gamma_i|} [\mathbf{n}_{ij} \cdot \mathbf{t}_k]^{\text{PNM}}, \quad (26)$$

where  $Q_{g,ij}$  denotes the gas phase volume flow rate through pore throat  $ij$ ,  $|\Gamma_i|$  is the area of the discrete coupling interface  $\Gamma_i$ , and  $\mathbf{n}_{ij}$  is a unit normal vector aligned with throat's central axis, pointing towards  $\Gamma_i$ . Potential deflections of the gas flow due the pore-body geometry are neglected and we assume that  $\Gamma_i$  is entirely occupied by the gas phase. There is a conceptual similarity of this pore-scale condition with the Beavers-Joseph interface slip condition widely used in REV-scale models (15, 44). The pore-scale slip parameter  $\beta_{\text{pore}}$  can be determined numerically in a preprocessing step (13).

The flux of each component  $\kappa$  is conserved across  $\Gamma_i$ ,

$$[(x_g^\kappa \varrho_{\text{mol},g} \mathbf{v}_g + \mathbf{j}_{\text{diff,mol},g}^\kappa) \cdot \mathbf{n}]^{\text{PNM}} = -[(x_g^\kappa \varrho_{\text{mol},g} \mathbf{v}_g + \mathbf{j}_{\text{diff,mol},g}^\kappa) \cdot \mathbf{n}]^{\text{FF}}. \quad (27)$$

Assuming local chemical equilibrium (15) within a pore body and at the interface,

$$[X_g^\kappa]^{\text{FF}} = [X_g^\kappa]^{\text{PNM}} \quad \text{on } \Gamma_i \quad (28)$$

is used as a Dirichlet-type coupling condition for  $\Omega^{\text{FF}}$ .

Fick's law approximates the diffusive molecular flux within the free-flow domain directly at the interface,

$$[\mathbf{j}_{\text{diff,mol},g}^\kappa \cdot \mathbf{n}]^{\text{FF}} = -\frac{1}{M^\kappa} [D_g \varrho_g]^{\text{FF+1}} \frac{[X_g^\kappa]^{\text{FF}} - [X_g^\kappa]^{\text{FF+1}}}{0.5[\Delta h]^{\text{FF+1}}}. \quad (29)$$

The superscript FF + 1 refers to quantities of the free-flow grid cell directly adjacent to the interface and  $0.5[\Delta h]^{\text{FF+1}}$  is the distance between that cell's center and the interface. All phase-transfer processes are assumed to occur within the interface pore body under local thermodynamic equilibrium. This implies that the vaporization takes places within the pore body. We restrict the effective transfer of water vapor from  $\Omega^{\text{PNM}}$  to  $\Omega^{\text{FF}}$  to diffusive and advective fluxes within the gas phase across  $\Gamma_i$ . We aim to include a condition allowing for liquid water to leave the network in future work. This could be relevant, e.g., for modeling hydrophobic materials such as fuel cell gas diffusion layers on top of which liquid droplets may form in  $\Omega^{\text{FF}}$ .

Energy is conserved across  $\Gamma_i$ ,

$$\begin{aligned} & \left[ \left( (h_g \varrho_g \mathbf{v}_g) + \sum_{\kappa} (\mathbf{j}_{\text{diff,mol,g}}^{\kappa} h_g^{\kappa}) - \lambda_g \nabla T \right) \cdot \mathbf{n} \right]^{\text{PNM}} \\ &= - \left[ \left( h_g \varrho_g \mathbf{v}_g + \sum_{\kappa} (\mathbf{j}_{\text{diff,mol,g}}^{\kappa} h_g^{\kappa}) - \lambda_g \nabla T \right) \cdot \mathbf{n} \right]^{\text{FF}} . \end{aligned} \quad (30)$$

Again, diffusive, conductive and convective energy transfer only occur through the gas phase. The conductive heat transfer is calculated in analogy to Eq. (29) by enforcing the continuity of temperatures on  $\Gamma_i$ ,

$$[T]^{\text{FF}} = [T]^{\text{PNM}} \quad \text{on } \Gamma_i . \quad (31)$$

### 2.3.2. Implementation and monolithic solver

We implemented the coupled model in DuMu<sup>x</sup>, an open-source toolbox for the simulation of flow and transport in permeable media (14, 45, 46) based on DUNE (47); `dune-foamgrid` (48) is used as network grid manager.

Figure 3 shows a flowchart of the model's algorithmic structure. Using a first order backward Euler scheme for the temporal discretization, Newton's method is used in each time step to linearize and solve the nonlinear system of equations. In doing so, a monolithic linear system comprising entries from both subdomains and the interface conditions is assembled into a single system matrix and passed to a direct linear solver. We employ a chopped variable update step with individual chopping factors for each primary variable in order to stabilize and speed-up convergence. At the end of each Newton iteration, the invasion state of each pore throat is checked (see Appendix A) and a primary variable switch, as described in Section 2.2.3, is invoked.

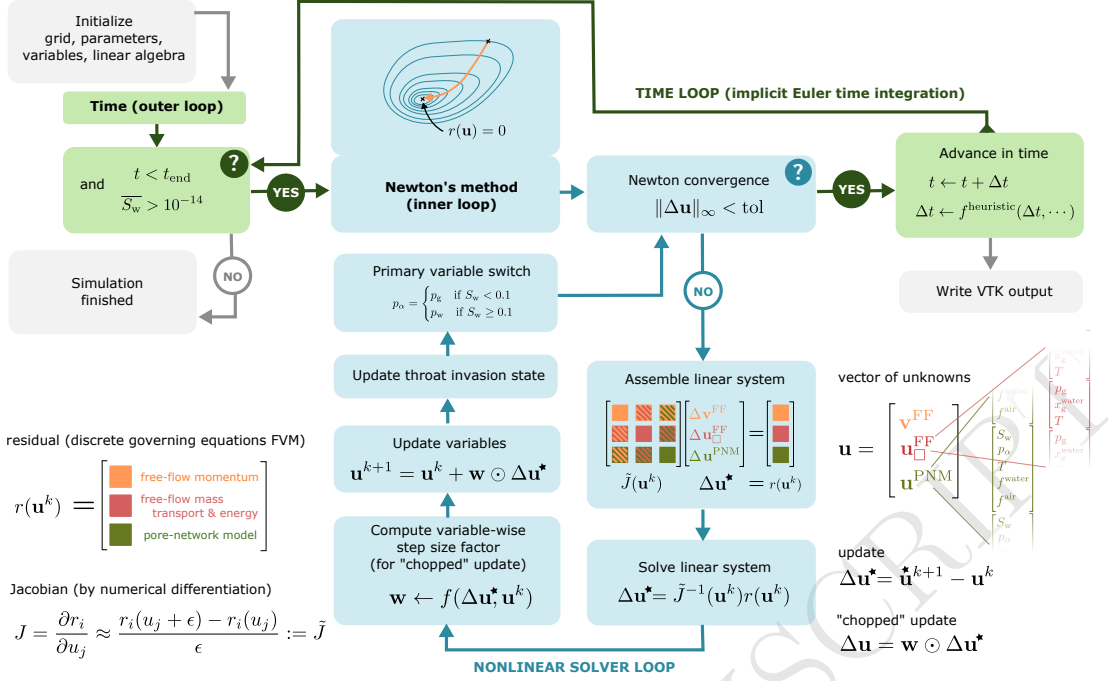


**Figure 3. Monolithic nonlinear solver scheme for coupled free-flow / pore-network model.** After the initialization of the grid (either generated on-the-fly or read-in from a file), an outer time loop (shown in green) is run until the averaged network saturation  $\bar{S}_w$  falls below a given threshold of  $1 \times 10^{-14}$ . In each time step, Newton's method (inner loop, shown in blue) is called in order to solve the nonlinear system of equations. All balance equations are assembled into one monolithic Jacobian matrix  $\tilde{J}$ . The vector of unknowns  $\mathbf{u}$  features a nested block structure holding the entries of each subdomain, taking into account the staggered-grid discretization scheme used for  $\Omega^{\text{FF}}$ .  $\mathbf{v}^{\text{FF}}$  stores all velocity unknowns located on the element faces of  $\Omega^{\text{FF}}$ .  $\mathbf{u}^{\text{FF}}$  holds all unknowns living on the cell centers of  $\Omega^{\text{FF}}$ . The unknowns of  $\Omega^{\text{PNM}}$  are stored in  $\mathbf{u}^{\text{PNM}}$ . We perform a chopped update step where  $\odot$  is a symbol for element-wise multiplication. After successful Newton convergence, the time loop advances the time step and optionally writes output files for visualization.

We chose the time step sizes heuristically based on the convergence rate of the Newton scheme,

$$\Delta t^{n+1} = \begin{cases} \Delta t^n \left( \frac{1}{1 + \frac{n_{\text{It},\text{target}} - n_{\text{It},\text{target}}}{n_{\text{It},\text{target}}}} \right) & n_{\text{It},\text{max}} > n_{\text{It}} > n_{\text{It},\text{target}}, \\ \Delta t^n \left( 1 + \frac{n_{\text{It},\text{target}} - n_{\text{It}}}{1.2n_{\text{It},\text{target}}} \right) & n_{\text{It}} \leq n_{\text{It},\text{target}} . \end{cases} \quad (32)$$

The number of Newton iterations required for the previous time step is given by  $n_{\text{It}}$  while  $n_{\text{It},\text{target}}$  is an input target value. The time step size is reduced by a given factor if  $n_{\text{It}}$  exceeds a given  $n_{\text{It},\text{max}}$ .

### 3. Numerical experiments

The presented PNM-FF model is applied in a range of different setups related to drying in porous media. In all cases, we consider a flat domain, resembling a microfluidic experimental device, cf. (49). Air in a gas channel ( $\Omega^{\text{FF}}$ ) flows past an initially water-saturated porous medium ( $\Omega^{\text{PNM}}$ ). We will investigate two general setups, one with a stagnant air atmosphere (Fig. 4(a) – referred to as scenario SA) and one with forced convective flow in the gas channel (Fig. 4(b) – referred to as scenario FC). The channel has a constant depth of  $d_{\text{ch}} = 400 \mu\text{m}$ . The remaining dimensions are given in Fig. 4(a). The flat nature of our setups justifies the use of a quasi-3D approach for the free-flow model and the neglect of gravity. We solve the two-dimensional Navier-Stokes equations with the wall-friction term given in Eq. (2). In a numerical preprocessing step, we determined  $\beta_{\text{pore}} = 3.71$  for Eq. (24) (13). The channel is discretized with  $133 \times 32$  axis-aligned rectangular cells in horizontal and vertical direction. We applied a spatial grading such that the vertical extend of the cells close to  $\Gamma$  and the upper boundary is smaller than in the rest of the domain. This allows to better approximate the velocity gradients at the channel boundaries.

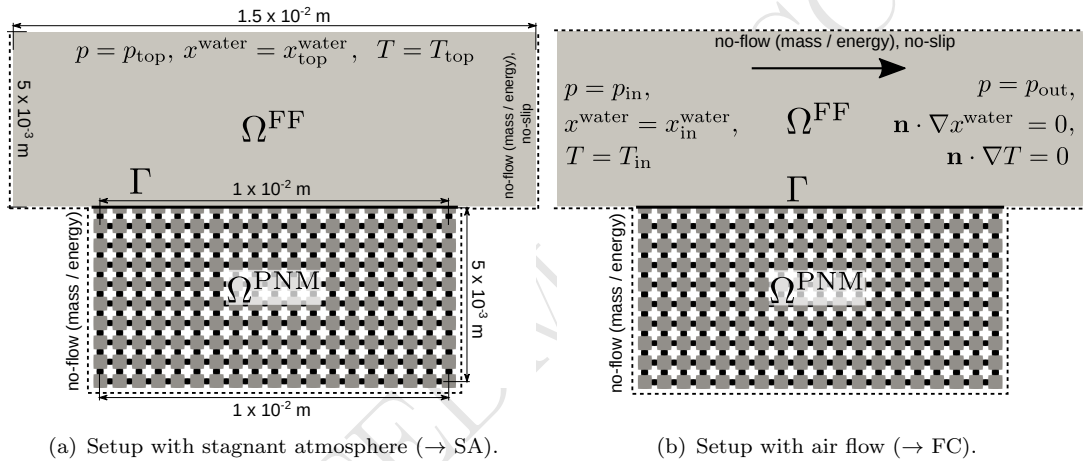


**Figure 4. Numerical experiment setup.** Water vapor will leave the system at the top of  $\Omega^{\text{FF}}$  in (a), while air flow from left to right in (b) will transport the vapor out of the system at the right boundary of  $\Omega^{\text{FF}}$ . The dimensions given in (a) also hold for (b), only the boundary conditions differ.

The pore network consists of  $19 \times 10$  equally spaced pores of cubic shape with log-normal-distributed inscribed pore body radii. The distribution parameters are given for each scenario. The pores are connected by throats of either quadratic, triangular or circular cross-sectional shapes with an inscribed radius based on the adjacent pore body radii, as described in Appendix B.

The numerical experiments are variations of the following basic scenario. The porous domain is initially fully saturated with the wetting phase,  $S_{w,\text{init}} = 1.0$ ,  $x_{w,\text{init}}^{\text{air}} = 1 \times 10^{-5}$ . The initial pressure and temperature are  $p_{g,\text{init}} = 1 \times 10^5 \text{ Pa}$  and  $T_{\text{init}} = 293.15 \text{ K}$  in both porous and free-flow domain. We initially start with 100 % relative humidity in the gas phase ( $x_{g,\text{init}}^{\text{water}} = 23.5 \times 10^{-3}$  at  $T = 293.15 \text{ K}$ ), but enforce a relative humidity of 20 % ( $x_{g,\text{top}}^{\text{water}} = x_{g,\text{in}}^{\text{water}} = 4.7 \times 10^{-3}$  at  $T = 293.15 \text{ K}$ ) on the top channel boundary or the channel inlet, respectively. In scenario SA (stagnant air) the channel sides (left, right, virtual back, virtual front) are insulated walls enforced by adiabatic, no-flow, no-slip boundary condition, and the initial and boundary values of

the gas velocity in the channel is  $\mathbf{v}_{g,\text{init}} = 0$ . The channel top is open but pressure, temperature and water vapor mole fraction are fixed. In scenario FC (forced convection), the channel top is closed for flow ( $\mathbf{v}_{g,\text{top}} = 0$ ) and a pressure gradient between left and right boundary ( $p_{\text{in}} = p_{\text{out}} + 1 \text{ Pa}$ ,  $p_{\text{out}} = 1 \times 10^5 \text{ Pa}$ , respectively) drives the gas flow yielding a maximum velocity of  $\mathbf{v} \approx 5 \times 10^{-2} \text{ m s}^{-1}$  in the channel and a Reynolds number of  $\text{Re} := \mathbf{v} d_{\text{ch}} \rho_g \mu_g^{-1} \approx 15$ , based on the channel height of  $d_{\text{ch}} = 5 \times 10^{-3} \text{ m}$ . The simulations are stopped once the domain-averaged saturation in  $\Omega^{\text{PNM}}$  is below  $1 \times 10^{-14}$  (fully-dried porous domain).

For the evaluation of the results, we define the total evaporation rate,

$$\dot{e} := \frac{\dot{m}^{\text{water}}}{\varrho_w |\Gamma|}, \quad (33)$$

as a global measure for characterizing the drying process. Here,  $\dot{m}^{\text{water}}$  is the total mass transfer rate of water from  $\Omega^{\text{PNM}}$  to  $\Omega^{\text{FF}}$  and  $|\Gamma|$  is the area of the entire interface  $\Gamma$  as show in Figs. 2(a) and 4, including both solid and pore spaces. The local specific vapor flow rate of a single pore  $i$  at a discrete coupling interface  $\Gamma_i$  is defined as

$$\varphi_i := \frac{\dot{m}_i^{\text{water}}}{\varrho_w |\Gamma_i|}, \quad (34)$$

where  $\dot{m}_i^{\text{water}}$  is the pore-local mass flux of water vapor across  $\Gamma_i$  and  $|\Gamma_i|$  is the area of the discrete coupling interface (see Fig. 2(b)).

## 4. Numerical results and discussion

### 4.1. Influence of pore throat shape and corner flow

The following numerical experiment investigates how the shape of the pore throats and the possibility of liquid phase corner flow affects the overall drying behavior. We consider scenario SA and three different pore networks with either quadratic, circular or triangular (equilateral) cross-sectional shapes. All pores in the left half of  $\Omega^{\text{PNM}}$  have a fixed inscribed radius of  $r_i = 2.2 \times 10^{-4} \text{ m}$  while those in the right half feature a slightly lower value of  $r_i = 2 \times 10^{-4} \text{ m}$  (radius distribution with zero variance) and therefore require a higher entry pressure.

Figure 5 shows the resulting wetting-phase saturation distribution and water vapor field for the setup with quadratic and circular pore throats after 5 and 25 hours of simulation time. The gas phase starts to invade the left half first because of the lower capillary entry pressure resulting from the larger pore throat radii, cf. Eq. (B1). Moreover, we observe that the invasion progresses fastest right at the interface between larger and smaller pores in the center of the domain. This is caused by capillary suction of finer pores on the right side of  $\Gamma$ , effectively pulling the liquid water towards to upper right. This phenomenon leads to faster drainage of the central pores and to a faster drying front progression.

For the case with circular throats (Figs. 5(a) and 5(c)), the pores in the left half dry out completely, resulting in a lower relative humidity in the channel above them. The gas channel interface is hydraulically disconnected from the bulk liquid phase once the circular throats have been invaded by the gas phase, completely displacing the liquid phase. This results in a significant decrease of the water transport rate (50) as the

evaporation process is then limited by diffusion of water vapor through the gas phase. There is still liquid water in the pores in the right half whose connecting throats have not been invaded by the gas phase yet. The cluster of invaded pores and throats on the left side features a gradient of saturation with the driest pores closest to the surface. Both parts of the porous medium get invaded more or less uniformly. The further the liquid phase recedes into the network, the larger the diffusion length (51) and the slower the evaporation process. In Fig. 5(c), the diffusive fluxes at the interface are higher on the right half of the network, where the liquid phase is still closer to the surface. The effect of diffusion length eventually balances out the initial advance of the gas phase within the left half.

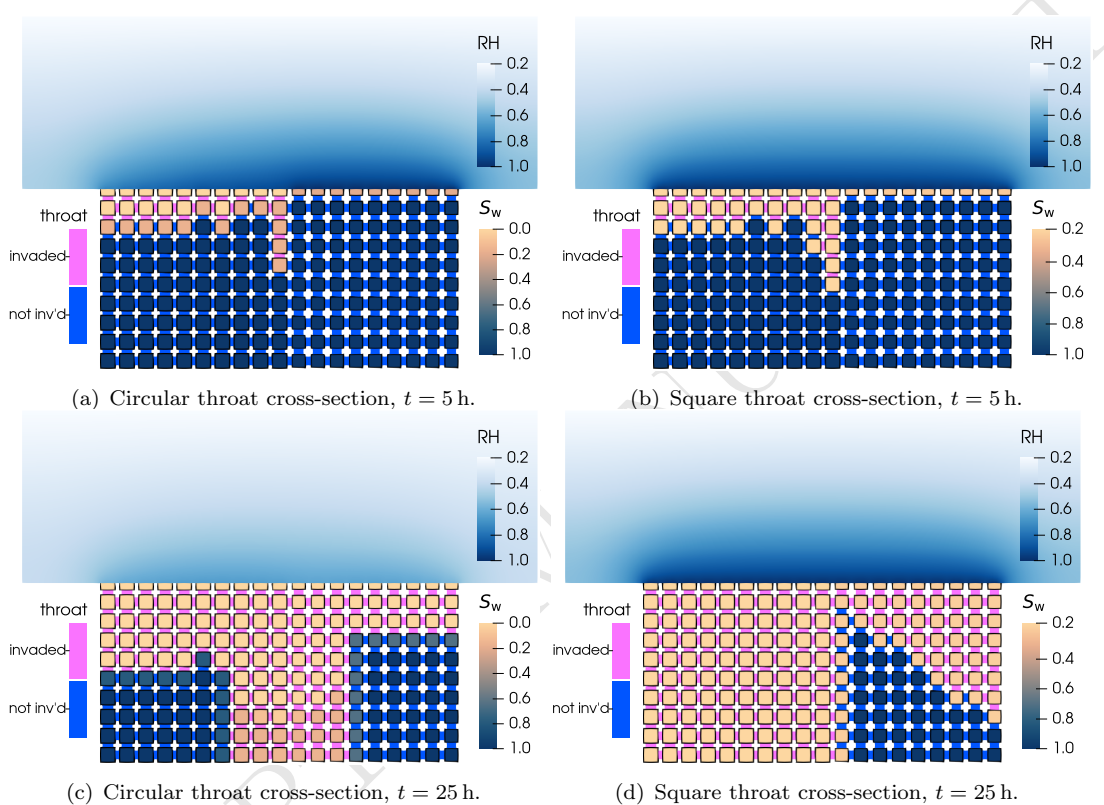


**Figure 5. Drying pattern for different throat cross-sectional shapes.** Drying under a stagnant atmosphere with circular (left column) or square (right column) pore throat cross-sections. Blue corresponds to a high wetting-phase saturation  $S_w$  within  $\Omega^{\text{PNM}}$  and a high relative humidity RH in  $\Omega^{\text{FF}}$ . Note the different color scales of  $S_w$  for square and circular throats: while some pores in (a) and (c) are completely dry, the presence of wetting layers in the square throats, shown in (b) and (d), facilitates the redistribution of water towards the surface such that the interface pores remain partly saturated ( $S_w = 0.2$ ). Throats marked in dark blue are fully occupied by the liquid phase while those in magenta are invaded by the air phase.

This is in contrast for the case with square throats, shown in Figs. 5(b) and 5(d). All pores within the gas phase cluster have the same liquid phase saturation of around 0.2 due to the effect of corner film flow. Corner flow ensures that wetting phase stays hydraulically connected throughout the domain. First, the entire left half of the network (featuring the larger pore bodies and lower capillary entry pressures) is invaded. Afterwards, the air progresses in the right half, where it spreads fastest at the right boundary due to the high pore-local vapor flow rate at the right corner interface pore. This pore shows the strongest water vapor concentration gradient in the adjacent free-flow region. We will discuss this effect in more detail in Section 4.2.

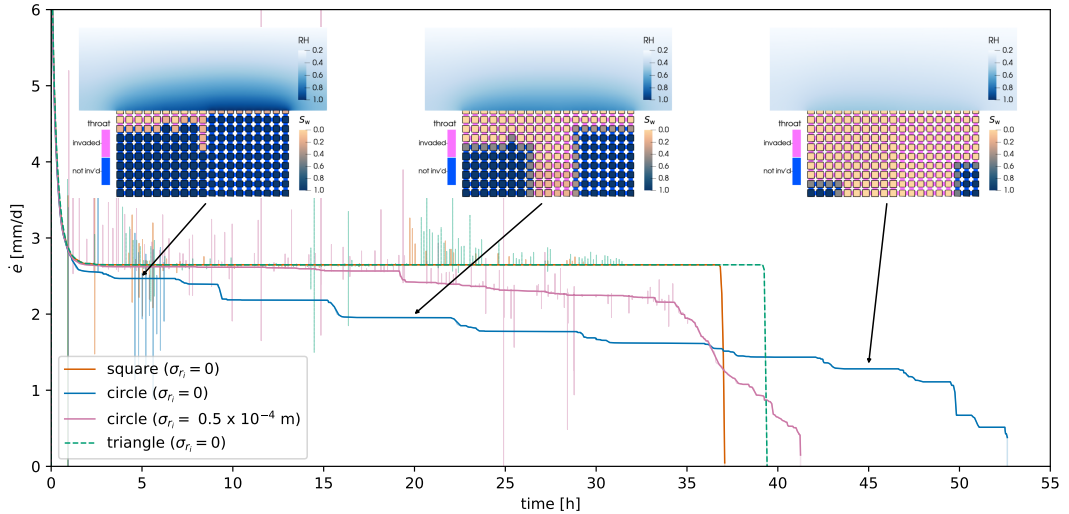


**Figure 6. Evaporation rates for different throat shapes (corner flow).** Global evaporation rates  $\dot{e}$  for networks with different throat shapes and a stagnant atmosphere. The inset figures show the wetting phase saturation  $S_w$  in  $\Omega^{\text{PNM}}$  and the relative humidity RH in  $\Omega^{\text{FF}}$  after 5, 20 and 45 hours for the case with circular throat cross sections. For all cases with  $\sigma_{r_i} = 0$ , the pore bodies have a fixed inscribed radius of  $r_i = 2.2 \times 10^{-4}$  m on the left half of the network and  $r_i = 2 \times 10^{-4}$  m on the right half of the domain. For the circle case, also the curve with a standard deviation of  $\sigma_{r_i} = 0.5 \times 10^{-4}$  m (applied to the inscribed pore body radii of both halves of the network) is shown (see Section 4.2). The curves have been smoothed using a median filter for ease of presentation. The thin, transparent lines show the original fluctuations which are caused by throat invasion events (see Fig. 10), leading to pressure spikes which typically level out after of some milliseconds and thus do not globally affect the cumulative evaporation rate. The vertical lines at the right end of the curves indicate the end of the simulation run.

The presence (or absence) of liquid water at  $\Gamma$  has important implications for the global evaporation rate  $\dot{e}$  shown in Fig. 6. All cases (square, circular or triangular throats) exhibit the same steep decrease of  $\dot{e}$  until approximately  $t = 1$  h due to equilibration processes at the interface (52). Following this,  $\dot{e}$  remains virtually constant for the square and triangular throats as a result of corner flow and the presence of liquid water at the surface. This corresponds to Stage-I (51) or constant-rate period evaporation (53). The sharp drop of  $\dot{e}$  at around  $t = 37$  h for the square throats marks the end of the drying process ( $S_w \rightarrow 0$ ).

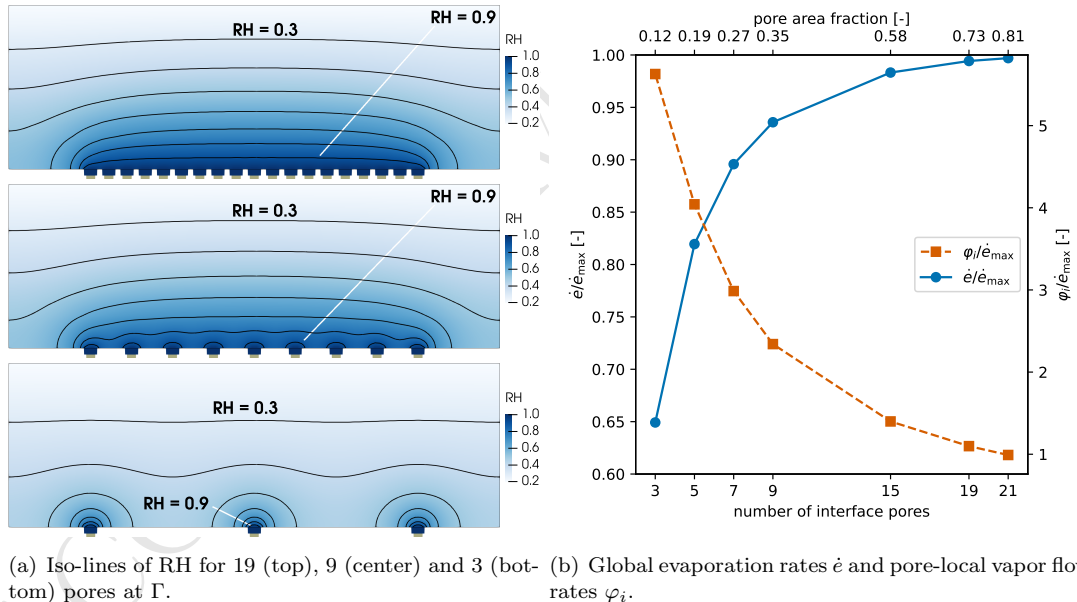
Using pore-network simulations, Prat (50) showed that the throat shape does not affect  $\dot{e}$  as long as liquid films remain connected to the surface of the porous medium. Our results for angular throats confirm this finding. The triangular throats feature the same constant global evaporation rate as the square shaped ones (see green dashed line in Fig. 6). Since we use the same inscribed radii  $r_{ij}$  for all shapes,  $A_{\text{tot},ij,\square} < A_{\text{tot},ij,\Delta}$  (see Fig. 1(b)) results in a slightly larger porosity for the network with triangular throats and therefore in longer drying times. For the chosen network size, liquid films are present throughout the entire domain at all times. The liquid films only start to disconnect for much larger networks. We could observe this effect when increasing the number of vertical pores to around 100 (not reported here) owing to capillary pressure gradients and the increase of cumulative liquid-phase flow resistance. In its current form, our model does not consider early film break-up as observed in experiments (7). It is a potentially interesting extension of the model to investigate mechanism and algorithms for film break-up based on experimental findings.

Changing from angular throats strongly affects the evaporation behavior.

Figure 6 shows a step-wise decrease of  $\dot{e}$  which can be attributed to the discrete increase of the total evaporation length (51) for each horizontal row of throats (see inset figures) invaded by the gas phase. All pores above the invaded throats dry out completely as the atmospheric demand exceeds the diffusive flux of water vapor through the invaded throats. In between the invasion events,  $\dot{e}$  remains virtually constant as the equilibrium water vapor concentration in the pores right below the newly invaded throats also remains essentially constant and only  $S_{w,i}$  in these pores decreases. This corresponds to Stage-II or falling-rate period evaporation which is characterized by the absence of liquid water at the porous medium surface. The latter also causes the relative humidity to decrease over time in the channel right above the surface. This is in contrast to the case with angular throats where the relative humidity remains constant due to the presence of liquid water at  $\Gamma$ .

#### 4.2. Influence of surface water distribution and network heterogeneity

Firstly, we consider scenario SA with homogeneous fixed inscribed pore radii  $r_i = 2 \times 10^{-4} \text{ m}$  (zero variance). While keeping all other dimensions constant, we vary the number of pores in horizontal direction to investigate how the spacing of pores at the coupling interface  $\Gamma$  influences the drying behavior. The throats have a square cross-section shape and we run the simulations until the vapor distribution in  $\Omega^{\text{FF}}$  has reached a steady state (constant Stage-I evaporation).



(a) Iso-lines of RH for 19 (top), 9 (center) and 3 (bottom) pores at  $\Gamma$ . (b) Global evaporation rates  $\dot{e}$  and pore-local vapor flow rates  $\varphi_i$ .

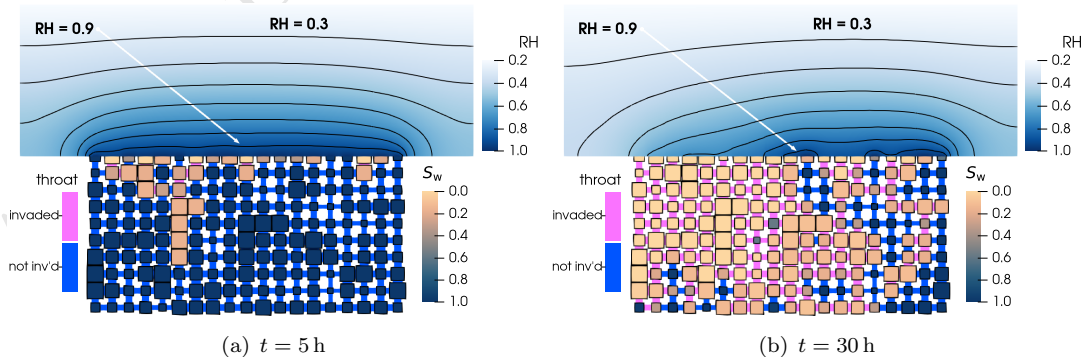
**Figure 7. External diffusional screening.** Fields and iso-lines of RH (a) and evaporation rates and vapor flow rates (b) for different pore spacings at the coupling interface  $\Gamma$  (square throats and stagnant atmosphere). The distances between the pores are  $\{0.16, 0.85, 4.6\} \text{ mm}$  for the cases with 19, 9 and 3 pores at  $\Gamma$ . The iso-lines closest to the pores correspond to RH = 0.9. For each line further away, RH decreases by 0.1. (b) shows the global and center-pore local vapor flow rates during Stage-I for setups with different numbers of pores at the interface. The evaporation rates and vapor flow rates are normalized by  $\dot{e}_{\max}$  which would occur if the entire area of  $\Gamma$  was occupied by a single, large water-filled pore. The pore area fraction is calculated as  $|\Gamma|^{-1} \sum_i |\Gamma_i|$ , where  $|\cdot|$  is the area of the (local) interface.

Figure 7(a) shows close-ups of  $\Omega^{\text{FF}}$  and  $\Gamma$  for 19, 9 and 3 pores at the interface. We

observe a clear difference in the resulting water vapor distribution above the pores: in the case with 19 pores, a rather uniform and almost one-dimensional field develops which only exhibits two-dimensional features at the left-most and right-most pores. There, the field gradient is highest, as shown by the narrow sequence of iso-lines. Increasing the spacing between the pores changes the vapor distribution such that the field becomes two-dimensional at each pore for the case with 3 pores at  $\Gamma$ . This also strongly increases the local vapor concentration gradient, leading to higher pore-local vapor flow rates, as illustrated in Fig. 7(b) where normalized global and pore-local vapor flow rates for different numbers of pores at  $\Gamma$  are given. For an increasing number of pores, the global evaporation rate converges against the value that would occur if the entire interfaces was occupied with water. The increase of the global evaporation rate  $\dot{e}$  with an increase of wetted surface at  $\Gamma$  follows a nonlinear trend (54) which is due to the previously mentioned change in the water vapor concentration field in  $\Omega^{\text{FF}}$ , leading to diminishing increases of  $\dot{e}$  once the vapor field becomes more or less one-dimensional. Reducing the number of pores at  $\Gamma$  on the other hand strongly increases the pore-local vapor flow rate due to the resulting two-dimensional, spherical nature of the vapor concentration field around the water-filled pores as shown by the dashed line in Fig. 7(b). This “external diffusional screening” (7) is a strong compensation effect such that  $\dot{e}$  decreases by less than 50% even if the number of interface pores is decreased from 21 to 3. This effect is expected to be even more pronounced in fully three-dimensional cases.

Secondly, we investigate this compensation effect in a heterogeneous network. We use scenario SA (this time in the reference setup with  $19 \times 10$  pores) and set a mean inscribed radius of  $r_i = 2.2 \times 10^{-4} \text{ m}$  to the pore bodies in the left half of the network, whereas the pores in the right half have a mean inscribed radius of  $r_i = 2.0 \times 10^{-4} \text{ m}$ . Unlike before, both pore radius distributions now feature a standard deviation of  $\sigma_{r_i} = 0.5 \times 10^{-4} \text{ m}$  (log-normal distribution).

The purple line in Fig. 6 shows the resulting global evaporation rate  $\dot{e}$ . The network dries out considerably faster compared to the case where  $\sigma_{r_i} = 0$  (41 h vs. 53 h). The evaporation rate remains almost constant for around 13 h (constant Stage-I evaporation) and decreases afterwards as some of the pores at the surface dry out. The surface remains partly wet until around 35 h. This is in contrast to the case with  $\sigma_{r_i} = 0$  where the evaporation front already recedes into the network after 10 h.



**Figure 8. Drying pattern for high pore-size variance.** Drying under a stagnant atmosphere with throat of circular section and  $\sigma_{r_i} = 0.5 \times 10^{-4} \text{ m}$ . Blue corresponds to a high wetting-phase saturation  $S_w$  within  $\Omega^{\text{PNM}}$  and a high relative humidity RH in  $\Omega^{\text{FF}}$ . Throats marked in dark blue are fully occupied by the liquid phase while those in magenta are invaded by the air phase.

The variability in pore and throat sizes at the surface causes a preferential invasion

of larger throats, while smaller pores and throats remain fully water-saturated for a prolonged time, see Fig. 8. This explains why  $\dot{e}$  drops slower in case of increased network heterogeneity. Furthermore, the curve is smoother because less throats get invaded simultaneously at a given time. In addition to the prolonged presence of liquid water at the surface, the increased network heterogeneity also elevates the pore-local vapor flow rates when neighboring pores fall dry. This is due to the previously discussed formation of spherical vapor concentration fields around the still water-saturated pores, as shown by relative humidity iso-lines in Fig. 8.

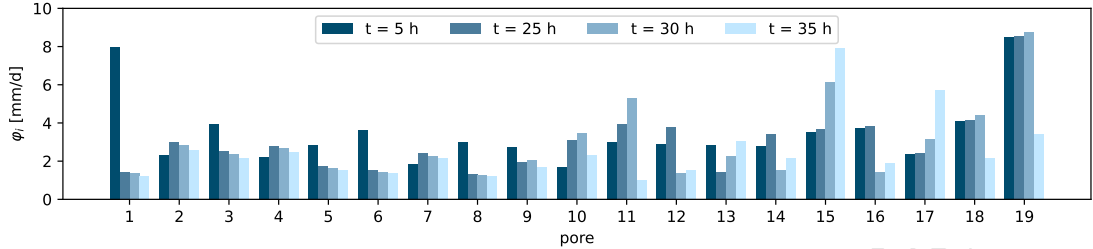


**Figure 9.** Temporal evolution of the pore-local vapor flow rates,  $\varphi_i$ , for all pores at the coupling interfaces  $\Gamma_i$  ( $i \in [1, 19]$ ) for the network with circular throats ( $\sigma_{r_i} = 0.5 \times 10^{-4}\text{ m}$ ) and stagnant air in  $\Omega^{\text{FF}}$ .

This effect is also visible in Fig. 9, showing the pore-local vapor flow rates  $\varphi_i$  over time for the network with increased heterogeneity. At  $t = 5\text{ h}$ , the highest local rates occur at the corner pores on the left and right side of  $\Gamma$ , as expected. The spatial fluctuations for the other pores are caused by the gas phase invasion pattern. For instance, the second and forth pore on the left feature a comparatively low value of  $\varphi_i$  because they have already dried out after  $5\text{ h}$ . As time progresses, more and more pores fall dry, leading to sharp local drops of  $\varphi_i$ . At the same time, however, some pores actually increase their local rate as their neighbors dry out. This is especially visible for pore 15 after  $30\text{ h}$  and  $35\text{ h}$ . This compensation mechanism and the prolonged presence of water at the surface lead an overall increase of the global evaporation rate compared to the case with less heterogeneity.

Having focused on the processes and fluxes directly at the coupling interface, we now turn our attention to the interior of the network. Figure 10 shows how the saturation pattern in  $\Omega^{\text{PNM}}$  changes after a throat was invaded by the gas phase for the case with high pore-size variance. The invasion leads to a sudden displacement of the liquid phase by the gas phase in the pore right below the invaded throat (marked with a red circle), such that the pore-local liquid phase saturation  $S_{w,i}$  drops from 1.0 to 0.46. The displaced liquid water exits the pore through the left, right and bottom throats, as indicated by the green cones, and leads to increased liquid phase fluxes also further away from the invaded throat. These fluxes in turn lead to a phase redistribution such that many pores actually gain in  $S_{w,i}$ , as indicated by the green numbers in Fig. 10. For instance,  $S_{w,i}$  in the pore marked with  $\star$  increases from 0.12 to 0.15. Even in the leftmost pore at the interface  $\Gamma$ , which is quite far away from the invaded throat, the pore-local saturation is increased from 0.24 to 0.25. The invasion event also influences the velocity field in  $\Omega^{\text{FF}}$ , as show by the black arrows in Fig. 10, leading to an interesting pattern: the displaced water moving upwards on the right itself displaces air in the partly saturated pores close to the interface. This air leaves the network, causing the local increase of vertical velocity in the channel. At the same time, the air protruding downwards into the network on the left side (yellow cones in Fig. 10) causes an inflow of gas from the channel into the network. The invasion event's impact on the pressure and velocity fields in both domains is very limited in time and typically

vanishes after several milliseconds.

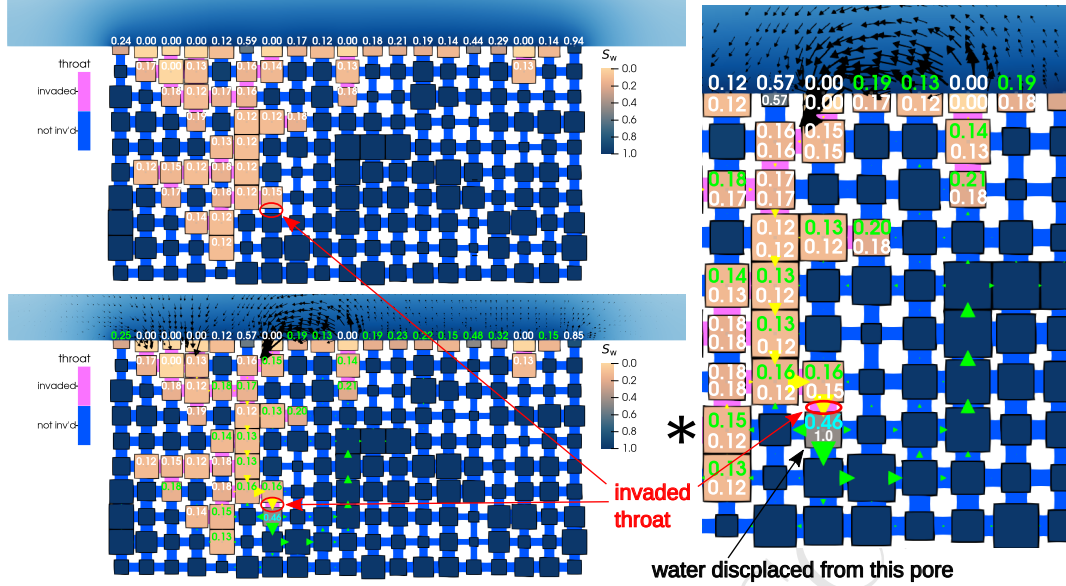


**Figure 10. Invasion event and redistribution of the liquid phase.** The top figure on the left shows the saturation distribution directly before an invasion event at around  $t = 9$  h, the figure below directly after the throat marked with the red circle was invaded by the gas phase. The figure on the right is a close-up of the region around the invaded throat. The yellow and green cones, scaled by  $Q_{g,ij}$  and  $Q_{w,ij}$ , indicate an increased flux of the gas and liquid phase. The numbers are the discrete values of  $S_{w,i}$ . Green numbers indicate an increase of pore-local saturation due to the invasion event. The top numbers in the right figure show the saturation after the invasion event, the bottom ones the saturation before. For example,  $S_{w,i}$  in the pore marked with \* rises from 0.12 to 0.15. The velocity vectors in the free-flow channel are scaled by magnitude.

#### 4.3. Influence of advective gas phase flow

We have seen in the previous section, that interesting local gas flow phenomena occur due to interaction of the porous and the free-flow region even for a stagnant atmosphere. In this section, we consider scenario FC, i.e. forced convection in the channel. We will examine two different cases: one with a uniform network of pores with  $r_i = 4 \times 10^{-4}$  m and one where the pore body inscribed radii follow a log-normal distribution with  $4 \times 10^{-4}$  m mean and  $0.5 \times 10^{-4}$  m standard deviation. This time, no distinction between the left and right half of the domain is made.

Figure 11 shows the progression of the drying process for the homogeneous and heterogeneous network under the influence of convective channel flow. A vapor concentration boundary layer forms above  $\Gamma$  right at the beginning of the process and remains essentially constant until the network completely dries out at around  $t \approx 16$  h for the homogeneous case and  $t \approx 17$  h for the heterogeneous case, see Figs. 11(g) and 11(h). In the channel, only at late times notable differences between the two cases can be observed. This is again due to the continuous presence of liquid water at the interface pores (corner flow), leading to a fully water-vapor-saturated gas atmosphere right above the pores. The temporal evolution of invasion pattern of the gas phase in  $\Omega^{\text{PNM}}$ , however, differs strongly between the two cases. At  $t = 1$  h, all pores at  $\Gamma$  are partly saturated in the homogeneous network and all but two connecting throats have already been invaded by the gas phase.

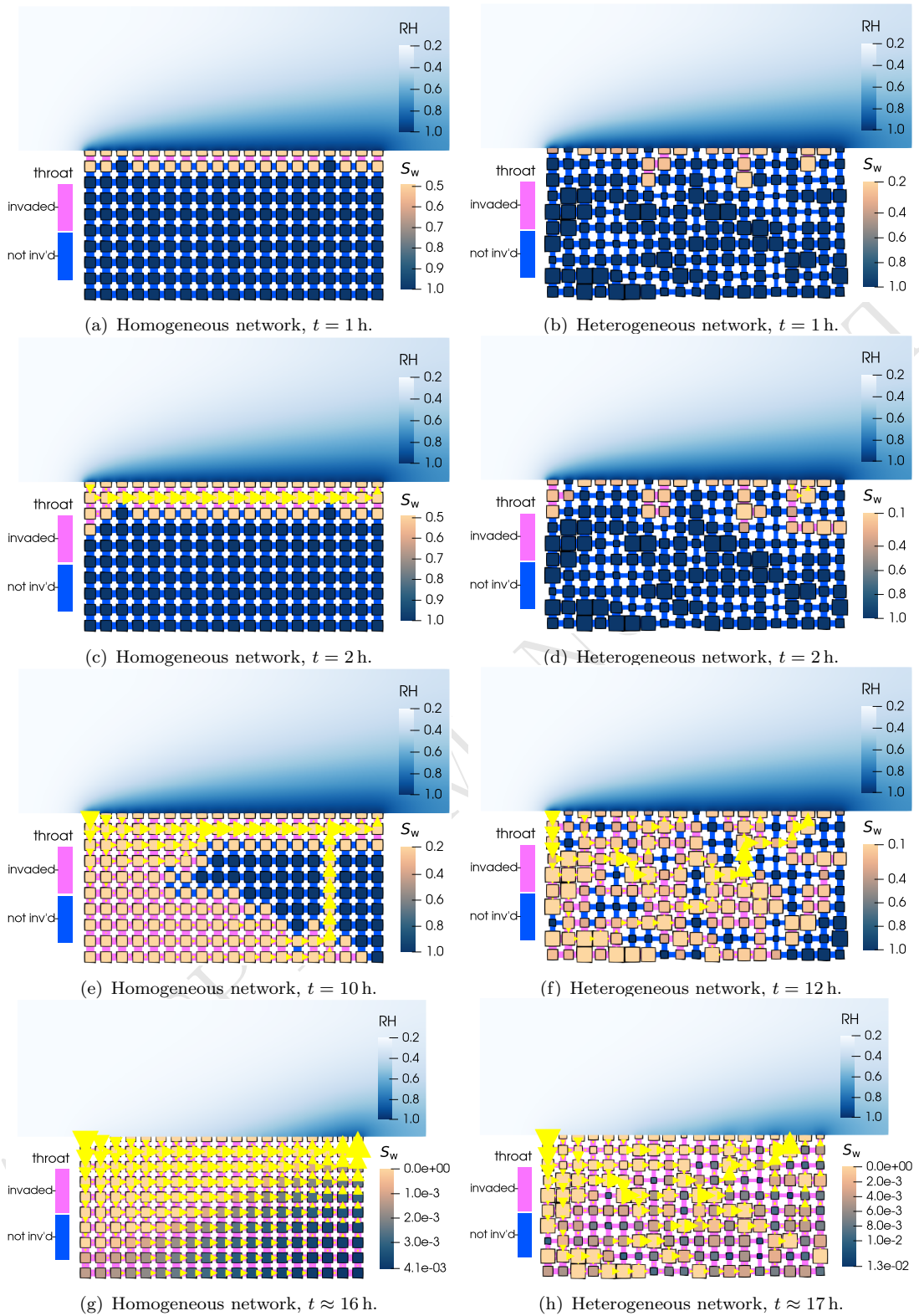


**Figure 11. Effect of gas phase flow: homogeneous vs. heterogeneous network.** Drying with convective channel flow for a uniform (left column) and heterogeneous (right column) network with square throats. Blue corresponds to a high wetting-phase saturation  $S_w$  within  $\Omega^{\text{PNM}}$  and a high relative humidity RH in  $\Omega^{\text{FF}}$ . Throats marked in dark blue are fully occupied by the liquid phase while those in magenta are invaded by the air phase. The yellow cones are scaled by  $Q_{g,ij}$  and indicate flow paths for the gas phase.

In contrast to that, six interface pores remained fully water-saturated in the heterogeneous case which can be explained by their comparatively small inscribed radius  $r_i$ , leading to a higher capillary pressure and stronger suction potential. As explained above, the throat radius correlates with the adjacent pore-body radii and we can observe that only wide throats connected to large pores have been invaded after one hour. The gas phase continues to spread mainly on the left side of the homogeneous network after  $t = 2$  h, Figs. 11(c) and 11(e), due to the highest pore-local vapor flow rates on the left, cf. Fig. 12(a). This is caused by the constant supply of warm dry air from the left. The dry air picks up water vapor as it streaks over the porous medium, leading to decreased pore-local vapor flow rates downstream.

The gas phase spreads differently in the heterogeneous network. Here, the invasion process is controlled by pore space geometry rather than by atmospheric demand. The difference in the gas-phase saturation distribution pattern has also consequences for the global evaporation rates, shown in Fig. 13. Here,  $\dot{e}$  remains virtually constant until around  $t = 11$  h (Stage-I evaporation). After that, the evaporation rate increases which seems unexpected at first glance.

For the homogeneous case, this effect occurs sooner and even more pronounced. The reason for this is the establishment of continuous flow paths for the air phase in  $\Omega^{\text{PNM}}$  which we could already observe in previous work (19). The air phase flows horizontally through the first row of invaded pores already after  $t = 2$  h for the homogeneous network, as shown by the yellow cones in Fig. 11(c). This leads to advective transport of water vapor within the network, effectively enhancing the mass transfer by pushing out the vapor as shown by the increase local rates for the three rightmost pores (17–19) in Fig. 12(a) at  $t = 2$  h.

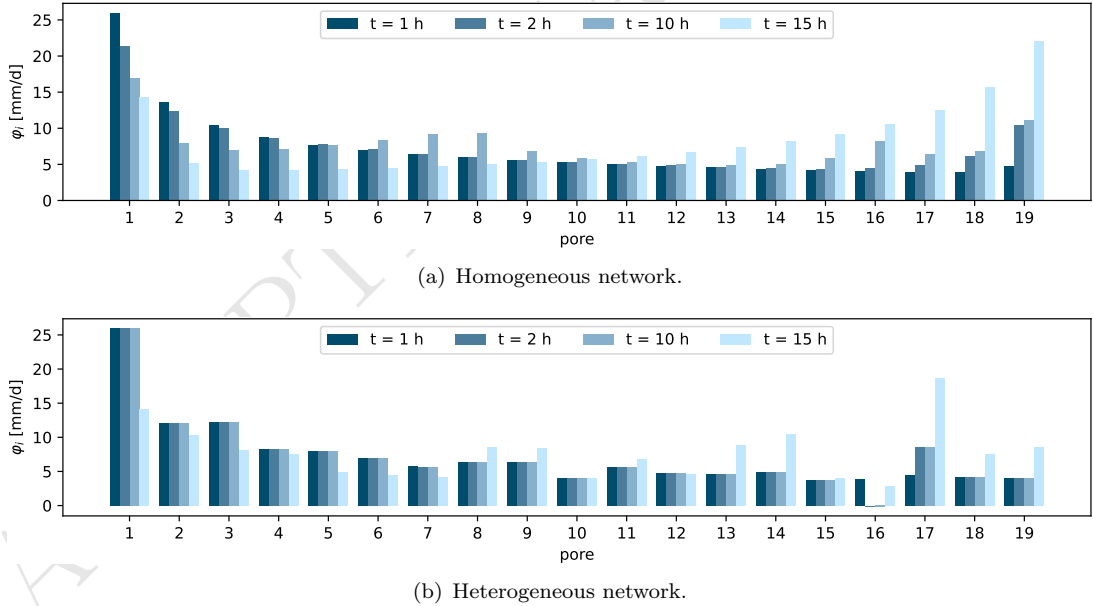


**Figure 12.** Temporal evolution of the pore-local vapor flow rates,  $\varphi_i$ , for all pores at the coupling interfaces  $\Gamma_i$  ( $i \in [1, 19]$ ) for the uniform (a) and heterogeneous (b) network with square throats and air flow in  $\Omega^{\text{FF}}$ .

At the same time, the local rates at the very left pores decrease due to the competing effect of advective air flow into the pore network and diffusion caused by the vapor concentration gradient in opposite direction. The absence of a continuous air flow

path until  $t = 11$  h in the heterogeneous network explains its constant evaporation rate since the advective effects described above do not come into play here yet. Some localized air flow effects are observed at pores 16 and 17, Figs. 11(d) and 12(b). At pore 16, the local vapor flow rate even becomes slightly negative, meaning that there is a net inflow of vapor into the network from the vapor concentration boundary layer due to advection. Finally, after  $t = 12$  h, the heterogeneous network also shows a well-developed but more complex air flow path, Fig. 11(f), leading to a slight increase of the global evaporation rate (Fig. 13).

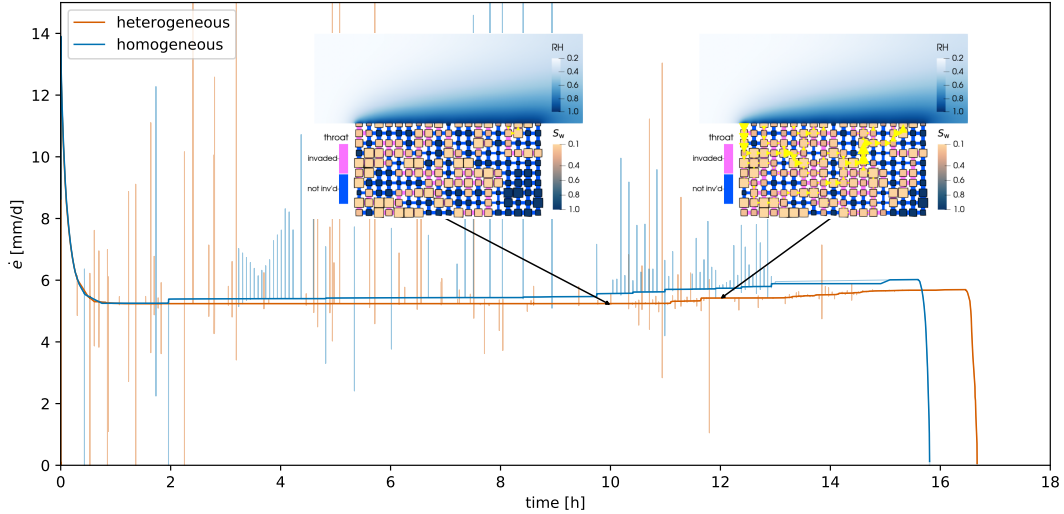


**Figure 13. Global evaporation rates: homogeneous vs. heterogeneous network.**  $\dot{e}$  for a uniform and a heterogeneous network with square throats and air flow in  $\Omega^{\text{FF}}$ . The inset figures show the wetting phase saturation  $S_w$  in  $\Omega^{\text{PNM}}$  and the relative humidity  $\text{RH}$  in  $\Omega^{\text{FF}}$  after 10 and 12 hours for the heterogeneous network. Here, a continuous air flow path develops after around 11 hours, leading to an increase of  $\dot{e}$  due to advective effects. Before that, the gas phase remains largely unconnected (left inset figure) such that  $\dot{e}$  also remains constant. Curves have been smoothed using a median filter for ease of presentation. The thin, transparent lines show the original fluctuations which are caused by throat invasion events. The vertical lines at the right end of the curves indicate the end of the simulation run.

In the final stage of the drying process, the interface pores dry out completely, Figs. 11(g) and 11(h), and the relative humidity above them drops rapidly. While the remaining amount of liquid water in  $\Omega^{\text{PNM}}$  ( $S_w \approx 1 \times 10^{-3}$ ) is distributed mainly on the right half of the homogeneous network due to advective effects, some singular small pores hold the residual water in the heterogeneous network due to capillary forces.

As initially mentioned in the introduction, instead of using a pre-calculated, fixed velocity field in  $\Omega^{\text{FF}}$  and neglecting the advective gas flow in the network (10, 11), we dynamically solve for  $\mathbf{v}_g$  and  $Q_{ij,g}$  in each time step. We have already seen that flow paths for the gas phase evolving in the network (Fig. 11) alter the evaporation behavior. Figure 14 shows that during the drying process, also the velocity distribution in  $\Omega^{\text{FF}}$  changes as the air phases intrude into the network. At  $t = 1$  h, no continuous pathway in the network has yet been established. The velocity profile, Fig. 14(b), is almost symmetric with the important exception that slip flow above the interface pores, cf. Eq. (24), leads to higher horizontal velocities at porous interface compared to the channel top. As described above, a horizontal gas flow path develops right beneath the surface of the network at  $t = 1$  h. As a consequence, a small fraction of the free

streaming air will bypass the channel through the network, effectively reducing the mean channel velocity right above  $\Omega^{\text{FF}}$ . As more and more throats get invaded, the portion of air traversing the network increases until after 15 h all throats are invaded and the free-flow velocity profile has noticeably tilted towards lower velocities near  $\Gamma$ .

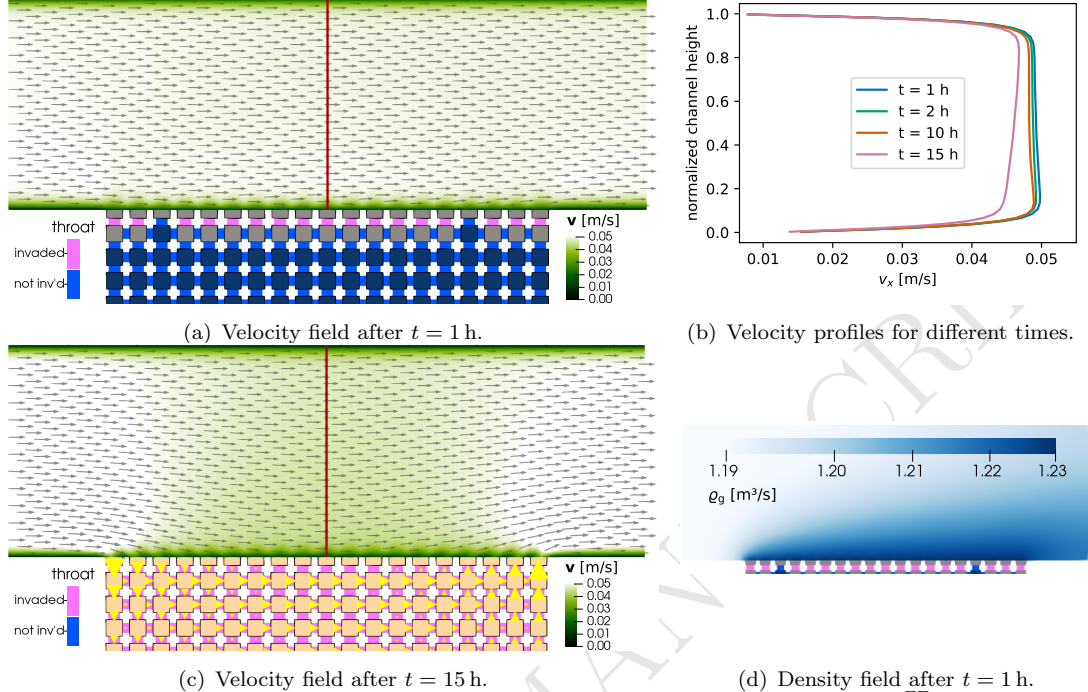


**Figure 14.** Free-flow velocity field and density. Change of the velocity field in  $\Omega^{\text{FF}}$  over time (a-c) and density field at  $t = 1$  h (d). (b) shows the horizontal velocity profiles evaluated along the red line in (a) and (c). There are no horizontal velocity degrees of freedom at the lower and upper wall of the channel when using the staggered grid discretization scheme in  $\Omega^{\text{FF}}$ , therefore the curve does not show values on the channel boundaries.  $v_x$  approaches zero at the upper wall (no-slip condition) while the slip-condition Eq. (25) leads to higher values right above the pores. At  $t = 15$  h the gas phase has fully penetrated the network which noticeably reduces the mean velocity in the channel and tilts the velocity profile towards lower velocities near the interface as a portion of the free air stream now bypasses the channel through the network. The yellow cones are scaled by  $Q_{g,ij}$  and indicate flow paths for the gas phase.

**Table 1.** Volume flow rates in  $\Omega^{\text{FF}}$  evaluated at the inlet and at the center (see red line in Fig. 14(a)) of channel.

time [h]	$Q_{g,\text{in}}^{\text{FF}} [1 \times 10^{-8} \text{ m}^3 \text{s}^{-1}]$	$Q_{g,\text{mid}}^{\text{FF}} [1 \times 10^{-8} \text{ m}^3 \text{s}^{-1}]$	$Q_{g,\text{mid}}^{\text{FF}}/Q_{g,\text{in}}^{\text{FF}} [-]$
1	9.58	9.43	0.98
2	9.72	9.35	0.96
10	9.88	9.26	0.94
15	10.27	8.77	0.85

Table 1 shows the temporal evolution of volume flow rates  $Q_g^{\text{FF}}$  at the inlet and at the center of the free-flow channel as well as their ratio. At  $t = 1$  h, the volume flow at the inlet is already 2% higher compared to the rate at the channel center despite the fact, that the gas phase does not yet flow in  $\Omega^{\text{PNM}}$ . This can be explained by the spatial variation of density, shown in Fig. 14(d), due to the change in temperature

caused by evaporative cooling. The increase in density above the network lowers the volume flow rate while the total mass flow rate is conserved (taking also into account the net mass transfer from  $\Omega^{\text{PNM}}$  to  $\Omega^{\text{FF}}$  due to evaporation). After  $t = 2$  h, air starts to flow through the network and with increasing time and number of invaded throats, the ratio  $Q_{\text{g,mid}}^{\text{FF}}/Q_{\text{g,in}}^{\text{FF}}$  rises until 15 % of the total gas volume flow bypasses the channel through the network. As this effectively also increases the systems total flow cross-sectional area, lowering the system's overall horizontal flow resistance, the inlet flow rate also rises since we keep the pressure boundaries conditions on the inlet and the outlet of the channel constant over time. This essentially increases the total flow of gas passing the inlet and outlet of  $\Omega^{\text{FF}}$  which, in combination with the advective gas flow in  $\Omega^{\text{PNM}}$ , eventually accelerates the drying process. The effects described above show the complex interaction between free flow and the porous domain which also changes over the duration of the drying process.

#### 4.4. *Model limitations and outlook*

While we could show that many physical effects are captured by the coupled PNM / free-flow model, we also want to point out current shortcomings of the model. As discussed above, the liquid corner films in angular throat do not break but rather become thinner and thinner and their conductivity approaches zero. In experiments (7), it is observed that films break when they reach a certain thickness, depending on the local geometry and fluid and solid properties. This effect should be explicitly considered in future work.

The effect of energy transport through the solid phase is currently not captured since we only considered the pore space in the network. We will address this issue in future work, using a dual network approach that also allows to resolve local thermal non-equilibrium between the solid and the fluid phase (18) which could become important for very fast drying processes.

Further planned model extensions include the effect of (salt) precipitation in the network and the interaction with turbulent free flow in combination with rough surfaces. We aim to validate our model based on microfluidic drying experiments. Furthermore, we plan to apply our model to setups presented in existing work (9–11) and provide a model comparison. It will be interesting to investigate cases where the pore-network acts as a block structure subject to frontal air flow. Here, stream-wise percolation paths of air could further enhance the advective gas transport within the network.

Finally, a drawback of the current approach is computational efficiency. Solving the Navier-Stokes equations including component and energy transport in the gas channel is costly. In combination with small time steps required by the pore-network model to resolve the complex physical flow processes in the network, this leads to significant cost. For instance, one of the simulations shown in Fig. 5 took several hours on an ordinary laptop (single core execution). However, we observed that apart from the local interactions around invasion events shown in Fig. 10, changes in velocity, density, temperature, and relative humidity only occur on slow time-scales. It is therefore conceivable to increase efficiency considerably by, for instance, only solving the free-flow velocity field after the occurrence of invasion effects. We note that care must be taken to ensure mass and energy conservation. In addition, we are working on parallelization to improve the model's performance. If the model can be sufficiently optimized, it will be interesting to recalculate drying experiments based on micro-tomography imaging data.

As a last note, we want to stress that model's degree of detail, e.g. with respect to temporal resolution, might seem exaggerated for certain real-world drying applications. However, we see it's true value in providing an in-depth physical insight into many complex, nonlinear and interacting effects. The possibility to create reference solutions not constrained by a rather large number of assumptions and simplifications, and the model's flexibility and extensibility, can help to improve and develop other, more efficient model concepts.

## 5. Conclusion

We have presented a fully coupled free-flow/pore-network model for simulating drying processes on the pore scale. The model is inherently mass and energy conservative and can provide detailed insights in the physical processes involved in drying. Applied to a range of setups inspired by microfluidic experiments, with each setup dedicated to a specific aspect of drying, the model was able to reproduce the relevant fundamental physical phenomena.

We have shown that the presence of corner flow in angular throats leads to higher and constant evaporation rates compared to a case with circular throats where the drying front recedes into the network. The spatial arrangement of water-filled pores at the surface of the porous domain strongly affects the pore-local vapor flow rates. The latter increases with larger distances between the interface pores as the one-dimensional structure of the water vapor concentration field changes to a spherical one above the pores, yielding larger concentration gradients and hence, diffusive fluxes. Considering a case with air flow above the network, we could observe how network heterogeneity influences the drying behavior both locally and globally. The establishment of continuous air-phase flow paths in the homogeneous network added another mechanism to the otherwise diffusion-controlled evaporation process: advective fluxes of the gas phase enhanced the transport of water vapor out of the pore network. With an increasing number of gas-phase invaded pores in the uniform network, the effect of advection became stronger, leading to a temporal increase of the global evaporation rate. In contrast to that, the evaporation rate remained constant for a much longer time in case of network heterogeneity which prevented to establishment of preferential gas phase flow paths such that advection only became important once the gas phase was able to connect the formerly disconnected patches of partly saturated pores in a later stage of the evaporation process. Only then, the global rate increased, too. The development of network gas flow paths also affects the free-flow domain such that the velocity does not remain constant but changes over time due air bypassing the free-flow channel through the network. We see our model concept presented here as a first important step towards a more detailed pore-scale description of drying processes.

### Code availability

A module containing the source code used to produce the numerical results is publicly available at <https://git.iws.uni-stuttgart.de/dumux-pub/weishaupt2021a>.

### **Acknowledgement(s)**

We thank the Deutsche Forschungsgemeinschaft (DFG, German Research Foundation) for supporting this work by funding SFB 1313, Project Number 327154368.

ACCEPTEDMANUSCRIPT

## References

- (1) Or, D.; Lehmann, P.; Shahraeeni, E.; Shokri, N. Advances in Soil Evaporation Physics—A Review, *Vadose Zone Journal* **2013**, *12* (4), 0.
- (2) Singh, A. Soil salinization and waterlogging: A threat to environment and agricultural sustainability, *Ecological Indicators* **2015**, *57*, 128–130.
- (3) Bonaui, C.; Dumoulin, E.; Raoult-Wack, A.L.; Berk, Z.; Bimbenet, J.; Courtois, F.; Trystram, G.; Vasseur, J. Food Drying and Dewatering, *Drying Technology* **1996**, *14* (9), 2135–2170.
- (4) Kemp, I.C. Fundamentals of Energy Analysis of Dryers. In *Modern Drying Technology*; Wiley-VCH Verlag GmbH & Co. KGaA, 2012; pp 1–45.
- (5) Defraeye, T. Advanced computational modelling for drying processes – A review, *Applied Energy* **2014**, *131*, 323–344.
- (6) Prat, M. Percolation model of drying under isothermal conditions in porous media, *International Journal of Multiphase Flow* **1993**, *19* (4), 691–704.
- (7) Prat, M. Pore Network Models of Drying, Contact Angle, and Film Flows, *Chemical Engineering & Technology* **2011**, *34* (7), 1029–1038.
- (8) Metzger, T. A personal view on pore network models in drying technology, *Drying Technology* **2018**, *37* (5), 497–512.
- (9) Shaeri, M.R.; Beyhaghi, S.; Pillai, K.M. On applying an external-flow driven mass transfer boundary condition to simulate drying from a pore-network model, *International Journal of Heat and Mass Transfer* **2013**, *57* (1), 331–344.
- (10) Xu, Z.; Pillai, K.M. Modeling drying in thin porous media after coupling pore-level drying dynamics with external flow field, *Drying Technology* **2016**, *35* (7), 785–801.
- (11) Xu, Z.; Pillai, K.M. A pore-network study on the factors influencing the isothermal drying of single- and dual-scale porous media, *Drying Technology* **2020**, 1–20.
- (12) Weishaupt, K.; Joekar-Niasar, V.; Helmig, R. An efficient coupling of free flow and porous media flow using the pore-network modeling approach, *Journal of Computational Physics: X* **2019**, *1*, 100011.
- (13) Weishaupt, K.; Terzis, A.; Zarikos, I.; Yang, G.; Flemisch, B.; de Winter, D.A.M.; Helmig, R. A Hybrid-Dimensional Coupled Pore-Network/Free-Flow Model Including Pore-Scale Slip and Its Application to a Micromodel Experiment, *Transport in Porous Media* **2020**, *135* (1), 243–270.
- (14) Koch, T.; Gläser, D.; Weishaupt, K.; Ackermann, S.; Beck, M.; Becker, B.; Burbulla, S.; Class, H.; Coltman, E.; Emmert, S.; et al. DuMux 3 – an open-source simulator for solving flow and transport problems in porous media with a focus on model coupling, *Computers & Mathematics with Applications* **2021**, *81*, 423–443.
- (15) Mosthaf, K.; Baber, K.; Flemisch, B.; Helmig, R.; Leijnse, A.; Rybak, I.; Wohlmuth, B. A coupling concept for two-phase compositional porous-medium and single-phase compositional free flow, *Water Resour. Res* **2011**, *47* (10).
- (16) Metzger, T.; Tsotsas, E. Viscous stabilization of drying front: Three-dimensional pore network simulations, *Chemical Engineering Research and Design* **2008**, *86* (7), 739–744.
- (17) Surasani, V.K.; Metzger, T.; Tsotsas, E. Drying Simulations of Various 3D Pore Structures by a Nonisothermal Pore Network Model, *Drying Technology* **2010**, *28* (5), 615–623.
- (18) Koch, T.; Weishaupt, K.; Müller, J.; Weigand, B.; Helmig, R. A (dual) network model for heat transfer in porous media: Towards efficient model concepts for coupled systems from fuel cells to heat exchangers, *Transport in Porous Media* **2021**. Accepted for publication.
- (19) Weishaupt, K.; Helmig, R. A dynamic and fully implicit non-isothermal, two-phase, two-component pore-network model coupled to single-phase free flow for the pore-scale description of evaporation processes, *Water Resources Research* **2021**, e2020WR028772. E2020WR028772 2020WR028772.
- (20) Wagner, W.; Prüß, A. The IAPWS Formulation 1995 for the Thermodynamic Properties of Ordinary Water Substance for General and Scientific Use, *Journal of Physical and Chemical Reference Data* **2002**, *31* (2), 387–535.

- (21) Reid, R.C.; Prausnitz, J.M.; Poling, B.E. *The properties of gases and liquids*, 4th ed.; McGraw Hill Book Co., New York, NY, 1987.
- (22) Flekkøy, E.G.; Oxaal, U.; Feder, J.; Jøssang, T. Hydrodynamic dispersion at stagnation points: Simulations and experiments, *Physical Review E* **1995**, *52* (5), 4952–4962.
- (23) Kunz, P.; Zarikos, I.M.; Karadimitriou, N.K.; Huber, M.; Nieken, U.; Hassanizadeh, S.M. Study of Multi-phase Flow in Porous Media: Comparison of SPH Simulations with Micro-model Experiments, *Transport in Porous Media* **2015**, *114* (2), 581–600.
- (24) Taylor, R.; Krishna, R. *Multicomponent mass transfer*; John Wiley & Sons, 1993; Vol. 2.
- (25) Harlow, F.H.; Welch, J.E. Numerical calculation of time-dependent viscous incompressible flow of fluid with free surface, *The Physics of Fluids* **1965**, *8* (12), 2182–2189.
- (26) Versteeg, H.K.; Malalasekera, W. *An introduction to computational fluid dynamics: the finite volume method*, 2nd ed.; Pearson Education: Harlow, 2007.
- (27) Schneider, M.; Weishaupt, K.; Gläser, D.; Boon, W.M.; Helmig, R. Coupling staggered-grid and MPFA finite volume methods for free flow/porous-medium flow problems, *Journal of Computational Physics* **2020**, *401*, 109012.
- (28) Joekar-Niasar, V.; Hassanizadeh, S.M.; Dahle, H.K. Non-equilibrium effects in capillarity and interfacial area in two-phase flow: dynamic pore-network modelling, *J. Fluid Mech.* **2010**, *655*, 38–71.
- (29) Qin, C. Water Transport in the Gas Diffusion Layer of a Polymer Electrolyte Fuel Cell: Dynamic Pore-Network Modeling, *Journal of The Electrochemical Society* **2015**, *162* (9), F1036–F1046.
- (30) Patzek, T.W.; Silin, D.B. Shape factor and hydraulic conductance in noncircular capillaries: I. One-Phase Creeping flow, *Journal of Colloid and Interface Science* **2001**, *236*, 295–304.
- (31) Mason, G.; Morrow, N.R. Capillary behavior of a perfectly wetting liquid in irregular triangular tubes, *Journal of Colloid and Interface Science* **1991**, *141* (1), 262–274.
- (32) Ransohoff, T.; Radke, C. Laminar flow of a wetting liquid along the corners of a predominantly gas-occupied noncircular pore, *Journal of Colloid and Interface Science* **1988**, *121* (2), 392–401.
- (33) Zhou, D.; Blunt, M.J.; Orr, F.M., Jr. Hydrocarbon Drainage along Corners of Noncircular Capillaries, *Journal of Colloid and Interface Science* **1997**, *187*, 11–21.
- (34) Bakke, S.; Øren, P.E. 3-D Pore-Scale Modelling of Sandstones and Flow Simulations in the Pore Networks, *SPE Journal* **1997**, *2* (02), 136–149.
- (35) Øren, P.E.; Bakke, S.; Arntzen, O. Extending Predictive Capabilities to Network Models, *SPE Journal* **1998**, *3* (04), 324–336.
- (36) Blunt, M.J. *Multiphase flow in permeable media: A pore-scale perspective*; Cambridge University Press: Cambridge, 2017.
- (37) Nuske, P.; Joekar-Niasar, V.; Helmig, R. Non-equilibrium in multiphase multicomponent flow in porous media: An evaporation example, *International Journal of Heat and Mass Transfer* **2014**, *74*, 128–142.
- (38) Maalal, O.; Prat, M.; Lasseux, D. Pore network model of drying with Kelvin effect, *Physics of Fluids* **2021**, *33* (2), 027103.
- (39) Class, H.; Helmig, R.; Bastian, P. Numerical simulation of non-isothermal multiphase multicomponent processes in porous media.: 1. An efficient solution technique, *Advances in Water Resources* **2002**, *25* (5), 533–550.
- (40) Class, H.; Helmig, R. Numerical simulation of non-isothermal multiphase multicomponent processes in porous media.: 2. Applications for the injection of steam and air, *Advances in Water Resources* **2002**, *25* (5), 551–564.
- (41) Lauser, A.; Hager, C.; Helmig, R.; Wohlmuth, B. A new approach for phase transitions in miscible multi-phase flow in porous media, *Advances in Water Resources* **2011**, *34* (8), 957–966.
- (42) Chen, B.; Chen, X.; Kanzow, C. A penalized Fischer-Burmeister NCP-function, *Mathematical Programming* **2000**, *88* (1), 211–216.
- (43) Chen, S.; Qin, C.; Guo, B. Fully Implicit Dynamic Pore-Network Modeling of Two-Phase

- Flow and Phase Change in Porous Media, *Water Resources Research* **2020**, *56* (11).
- (44) Beavers, G.S.; Joseph, D.D. Boundary conditions at a naturally permeable wall, *Journal of Fluid Mechanics* **1967**, *30* (01), 197–207.
  - (45) Flemisch, B.; Darcis, M.; Erbertseder, K.; Faigle, B.; Lauser, A.; Mosthaf, K.; Müthing, S.; Nuske, P.; Tatomir, A.; Wolff, M.; et al. DuMux: DUNE for multi-{phase, component, scale, physics, ... } flow and transport in porous media, *Advances in Water Resources* **2011**, *34* (9), 1102–1112.
  - (46) Weishaupt, K.; Class, H.; Coltrman, E.; Emmert, S.; Flemisch, B.; Gläser, D.; Grüninger, C.; Heck, K.; Jupe, T.; Kelm, M.; et al. DuMux 3.3.0, 2020.
  - (47) Bastian, P.; Blatt, M.; Dedner, A.; Dreier, N.A.; Engwer, C.; Fritze, R.; Gräser, C.; Grüninger, C.; Kempf, D.; Klöfkorn, R.; et al. The Dune framework: Basic concepts and recent developments, *Computers & Mathematics with Applications* **2021**, *81*, 75–112.
  - (48) Sander, O.; Koch, T.; Schröder, N.; Flemisch, B. The Dune FoamGrid implementation for surface and network grids, *Archive of Numerical Software* **2017**, *5* (1), 217–244.
  - (49) Terzis, A.; Zarikos, I.; Weishaupt, K.; Yang, G.; Chu, X.; Helmig, R.; Weigand, B. Microscopic velocity field measurements inside a regular porous medium adjacent to a low Reynolds number channel flow, *Physics of Fluids* **2019**, *31* (4), 042001.
  - (50) Prat, M. On the influence of pore shape, contact angle and film flows on drying of capillary porous media, *International Journal of Heat and Mass Transfer* **2007**, *50* (7-8), 1455–1468.
  - (51) Lehmann, P.; Assouline, S.; Or, D. Characteristic lengths affecting evaporative drying of porous media, *Physical Review E* **2008**, *77* (5).
  - (52) Mosthaf, K.; Helmig, R.; Or, D. Modeling and analysis of evaporation processes from porous media on the REV scale, *Water Resources Research* **2014**, *50* (2), 1059–1079.
  - (53) Yiotis, A.G.; Tsipanogiannis, I.N.; Stubos, A.K.; Yortsos, Y.C. Pore-network study of the characteristic periods in the drying of porous materials, *Journal of Colloid and Interface Science* **2006**, *297* (2), 738–748.
  - (54) Shahraeeni, E.; Lehmann, P.; Or, D. Coupling of evaporative fluxes from drying porous surfaces with air boundary layer: Characteristics of evaporation from discrete pores, *ources Research* **2012**, *48* (9).

## Appendix A. Capillary entry pressure

The capillary entry pressure that has to be overcome to invade a pore throat saturated with the wetting fluid is given by (36)

$$p_{c,e} = \frac{\gamma \left(1 + 2\sqrt{\pi G}\right) \cos(\theta) F_d(\theta, G)}{r_{ij}} , \quad (\text{A1})$$

$$F_d(\theta, G) = \frac{1 + \sqrt{1 + 4GE/\cos^2(\theta)}}{1 + 2\sqrt{\pi G}} , \quad (\text{A2})$$

$$E = \pi - 3\theta + 3\sin(\theta)\cos(\theta) - \frac{\cos^2(\theta)}{4G} , \quad (\text{A3})$$

where  $\theta$  denotes the contact angle,  $\gamma$  is the interfacial tension,  $F_d(\theta, G)$  is a dimensionless correction factor which becomes 1 for  $\theta = 0$ , and  $G$  is the shape factor introduced in Eq. (10).

If the capillary pressure falls below

$$p_{c,s} = \frac{\gamma \cos(\theta)}{r_{ij}} (1 - \tan(\theta) \tan(\beta)) \quad (\text{A4})$$

snap-off occurs (36) and the throat is saturated again by the wetting phase. Here  $\beta$  is the corner half-angle (assuming square or equilateral triangle cross-sectional shapes). We always consider  $\max(p_{c,i}, p_{c,j})$  to determine snap-off processes.

## Appendix B. Inscribed throat radius

The inscribed throat radius  $r_{ij}$  depends on the adjacent pore body radii  $r_i$  and  $r_j$  (28):

$$r_{ij} = d_{ij} \zeta_i \zeta_j \left( \zeta_i^{1/n} + \zeta_j^{1/n} \right)^{-n}, \quad n > 0 \quad (\text{B1})$$

$$\zeta_k = \frac{r_k d_{ij}^{-1} \sin(\pi/4)}{\left( 1 - r_k d_{ij}^{-1} \cos(\pi/4) \right)^n}, \quad k \in \{i, j\}, \quad (\text{B2})$$

where  $d_{ij}$  is the pore center-to-center distance and  $n$  controls the scaling between  $r_{ij}$  and the adjacent pore body radii. We chose  $n = 0.1$  in this work.